

1 **Improving PM_{2.5} forecast over China by the joint adjustment of initial conditions**
2 **and source emissions with an ensemble Kalman filter**

3 Zhen Peng^{1,2}, Zhiquan Liu², Dan Chen², Junmei Ban²

4 1 School of Atmospheric Sciences, Nanjing University, Nanjing, China

5 2 National Center for Atmospheric Research, Boulder, Colorado, USA

6
7 **Abstract.** In an attempt to improve the forecasting of atmospheric aerosols, the
8 ensemble square root filter algorithm was extended to simultaneously optimize the
9 chemical initial conditions and emission input. The forecast model, which was
10 expanded by combining the Weather Research and Forecasting with Chemistry
11 (WRF-Chem) model and a forecast model of emission scaling factors, generated both
12 chemical concentration fields and emission scaling factors. The forecast model of
13 emission scaling factors was developed by using the ensemble concentration ratios of
14 the WRF-Chem forecast chemical concentrations and also the time smoothing
15 operator. Hourly surface fine particulate matter (PM_{2.5}) observations were assimilated
16 in this system over China from 5 to 16 October 2014. A series of 48-h forecasts were
17 then carried out with the optimized initial conditions and emissions on each day at
18 0000 UTC and a control experiment was performed without data assimilation. Besides,
19 we also performed an experiment of pure assimilation chemical ICs and the
20 corresponding 48-h forecasts experiment for comparison. The results showed that the
21 forecasts with the optimized initial conditions and emissions typically outperformed
22 those from the control experiment. In the Yangtze River delta (YRD) and the Pearl
23 River delta (PRD) regions, large reduction of the Root Mean Square Errors (RMSEs)
24 was obtained for almost the entire 48-h forecast range attributed to assimilation.

25 Especially, the relative reduction in RMSE due to assimilation was about 37.5% at
26 nighttime when WRF-Chem performed comparatively worse. In the Beijing–Tianjin–
27 Hebei (JJJ) region, relatively smaller improvements were achieved in the first 24-h
28 forecast. Comparing to the forecasts with only the optimized ICs, the forecasts with
29 the joint adjustment were always much better for almost all the forecasts in the PRD
30 and YRD, although they were very similar in the JJJ region.

31

32 **1. Introduction**

33 Aerosol prediction by regional air quality model in heavy polluted regions is
34 challenging due to many factors. In addition to the deficiency of chemistries, the
35 uncertainties of primary and precursor emissions and the initial conditions (ICs) also
36 limit the forecast accuracy. Data assimilation (DA), which is used to improve the ICs
37 of aerosols and to optimize data on aerosol emissions, has been shown to be one of
38 the most effective ways to improve the forecasting of aerosol pollution.

39 From the perspective of reducing the uncertainties in the ICs for aerosols, recent
40 efforts have focused on assimilating aerosol observations using optimal interpolation
41 (Collins et al., 2001; Yu et al., 2003; Adhikary et al., 2008; Tombette et al., 2009; Lee
42 et al., 2013) or variational (Kahnert, 2008; Zhang et al., 2008; Benedetti et al., 2009;
43 Pagowski et al., 2010; Liu et al., 2011; Schwartz et al., 2012; Li et al., 2013; Jiang et
44 al., 2013; Saide et al., 2013) DA algorithms. Ensemble-based DA algorithms, such as
45 the ensemble Kalman filter (EnKF) (Sekiyama et al., 2010; Schutgens et al., 2010a,
46 2010b; Pagowski and Grell, 2012; Dai et al., 2014; Rubin et al., 2016; Ying, X.M., et
47 al., 2016; Yumimoto et al., 2016) and the hybrid variational-ensemble DA approach
48 (Schwartz et al., 2014) have also been applied to aerosol predictions. All these studies
49 have shown that DA is one of the most effective ways of improving aerosol
50 forecasting through assimilating aerosol observations from multiple sources (e.g.
51 ground-based observations and satellite measurements) to update the chemical ICs.

52 Numerous studies have used DA approaches to estimate or improve source

53 emissions. The EnKF is one of the most popular DA algorithms used to improve
54 estimates of aerosols and gas-phase emissions, such as NO_x, volatile organic
55 compounds, and SO₂ (van Loon et al., 2000; Heemink and Segers, 2002; Zhang et al.,
56 2005; Barbu et al., 2009; Sekiyama et al., 2010; Huneus et al., 2012; Schutgens et al.,
57 2012; Huneus et al., 2012, 2013; Miyazaki et al., 2014). Variational DA algorithms
58 have also been applied to constrain emissions of air pollution, such as black carbon,
59 organic carbon, dust, NH₃, SO_x and NO_x (Hakami et al., 2005; Elbern et al., 2007;
60 Henze et al., 2007, 2009; Yumimoto et al., 2007, 2008; Dubovik et al., 2008; Wang et
61 al., 2012; Guerrette and Henze, 2015). These studies have indicated that DA can
62 efficiently reduce the uncertainty in the emission inventories and lead to
63 improvements in the forecasting of air quality (Mijling and van der A, 2012).

64 The optimization of chemical ICs and pollution emissions can improve aerosol
65 forecasts and therefore further improvements are likely to be achieved by
66 simultaneously optimizing the chemical ICs and emissions. Tang et al. (2011)
67 reported that the simultaneous adjustment of the ICs of O₃, NO_x and volatile organic
68 compounds and the emissions of NO_x and volatile organic compounds produced
69 overall better performance in both the 1-h and 24-h ozone forecasts than the
70 adjustment of pure ICs or emissions. Miyazaki et al. (2012) reported that the
71 simultaneous adjustment of emissions and concentrations is a powerful approach to
72 correcting the tropospheric ozone budget and profile analyses.

73 We developed a system to adjust the chemical ICs and source emissions jointly
74 within an EnKF system coupled to the Weather Research and Forecasting with
75 Chemistry (WRF-Chem) model (Grell et al., 2005). We then applied this system to
76 assimilate hourly surface PM_{2.5} measurements over China in early October 2014.

77 The remainder of the paper is organized as follows. Section 2 describes this DA
78 system in detail and Section 3 describes the PM_{2.5} observations. Then the
79 experimental designs are introduced in Section 4. Finally, the surface PM_{2.5}
80 observations assimilation results are presented in section 5 before concluding in
81 section 6.

82

83 **2. Methodology**

84 **2.1 Forecast model**

85 For a chemical model like WRF-Chem, the emissions are the model forcing (or
86 boundary condition), rather than model states. Therefore, a forecasting model, **M**,
87 was developed to forecast the emission scaling factors (representing emissions) as
88 well as the aerosol concentrations. This model combines the WRF-Chem model and
89 the forecast model of emission scaling factors.

90

91 2.1.1 WRF-Chem model

92 Version 3.6.1 of the WRF-Chem model (Grell et al., 2005) was used to forecast the
93 aerosol and chemical species. WRF-Chem is an online model with the fully coupled
94 chemical and meteorological components.

95 Most of the WRF-Chem settings were the same as those reported in Liu et al.
96 (2011): the Goddard Chemistry Aerosol Radiation and Transport (GOCART) aerosol
97 scheme coupled with the Regional Atmospheric Chemistry Mechanism for gaseous
98 chemical mechanisms; the WRF single-moment five-class microphysics scheme; the
99 Rapid Radiative Transfer Model longwave and Goddard shortwave radiation schemes;
100 the Yonsei University (YSU) boundary layer scheme; the Noah land surface model;
101 and the Grell-3D cumulus parameterization. For the GOCART aerosol scheme, the
102 aerosol species include 14 defined aerosol species and a 15th variable representing
103 unspatiated aerosol contributions (P_{25}). The 14 defined aerosol species are sulfate,
104 hydrophobic and hydrophilic organic carbon (OC_1 and OC_2 , respectively),
105 hydrophobic and hydrophilic black carbon (BC_1 and BC_2 , respectively), dust in five
106 particle size bins (effective radii of 0.5, 1.4, 2.4, 4.5 and 8.0 μm ; referred to as D_1 ,
107 D_2 , D_3 , D_4 and D_5 , respectively) and sea salt in four particle size bins (effective
108 radii of 0.3, 1.0, 3.25 and 7.5 μm for dry air; referred to as S_1 , S_2 , S_3 and S_4 ,
109 respectively).

110 Figure 1 illustrates the model computational domain. It has 120*120 horizontal
111 grid scales at a 40.5 km spacing by the Lambert conform map projection centered at
112 (35 °N, 105 °E). There are 57 vertical levels with the model top at 10 hPa, about 12

113 layers within the planetary boundary layer (among them the lowest 8 layers were
114 under 500 m), and the first layer centered at ~12 m.

115 With respect to the emissions, the hourly prior anthropogenic emissions were
116 based on the monthly regional emission inventory in Asia (Zhang et al., 2009) for the
117 year 2006 interpolated to the model grid. The power generator emissions were
118 interpolated for the lowest eight vertical levels (Woo et al., 2003; de meij et al., 2006;
119 Wang et al., 2010). Other anthropogenic emissions were assigned totally to the 1st
120 level. Emissions are very small above 500 m for all pollutants. In order to keep
121 objective for the prior anthropogenic emissions, no time variation was added. Thus,
122 the hourly prior anthropogenic emissions were constant. The biogenic (Guenther et al.,
123 1995), dust (Ginoux et al., 2001), dimethylsulfide and sea salt emissions (Chin et al.,
124 2000, 2002) were calculated online.

125

126 2.1.2 Forecast model of scaling factors

127 As no suitable dynamic model was available to forecast the emission scaling factors, a
128 persistence forecasting operator served as the forecast model for the scaling factors,
129 similar to the method used by Peng et al. (2015) for CO₂ emission inversion. Figure
130 2a shows the flowchart for the persistence forecasting operator \mathbf{M}_{SF} .

131 If the ensemble members of the updated chemical fields $\mathbf{C}_{i,t-1}^a$ (the subscript i
132 refers to the i th ensemble member, the superscript a refers to the analysis, and t
133 refers to the time) and the forecast emissions $\mathbf{E}_{i,t-1}^f$ (the superscript f refers to the
134 forecast) in the previous assimilation cycle are known, then the chemical fields $\mathbf{C}_{i,t}^f$
135 at time t can be generated via WRF-Chem (Figure 2b). In the actual process, $\mathbf{C}_{i,t}^f$
136 were available in the previous assimilation cycle, so we did not need to perform the
137 ensemble forecasts again. A dotted box was used in Figure 2a to indicate that the
138 ensemble forecasts were not performed in real process. The ensemble concentration
139 ratios $\kappa_{i,t}$, ($i = 1, \dots, N$) are then calculated using

$$140 \quad \kappa_{i,t} = \frac{\mathbf{C}_{i,t}^f}{\bar{\mathbf{C}}_t^f}, (i = 1, \dots, N), (1)$$

141 where $\bar{\mathbf{C}}_t^f = \frac{1}{N} \sum_{i=1}^N \mathbf{C}_{i,t}^f$ is the ensemble mean of the forecast. The ensemble mean of

142 $\kappa_{i,t}$ is,

$$143 \quad \overline{\kappa}_t = \frac{1}{N} \sum_{i=1}^N \kappa_{i,t} = \frac{1}{N} \sum_{i=1}^N \mathbf{C}_{i,t}^f / \overline{\mathbf{C}_t^f} = 1, (2)$$

144 so $\kappa_{i,t}$ are numbers distributed around 1 and with ensemble mean values of 1.

145 The ensemble spreads of $\kappa_{i,t}, (i = 1, \dots, N)$ may be small and therefore
146 covariance inflation is used to maintain them at a certain level:

$$147 \quad (\kappa_{i,t})_{\text{inf}} = \beta(\kappa_{i,t} - \overline{\kappa}_t) + \overline{\kappa}_t, (i = 1, \dots, N), (3)$$

148 In Peng et al. (2015), the CO₂ DA system worked comparatively well when the
149 ensemble spread of $\lambda_{i,t}^a$ ranged from 0.05 to 1.25 for $\beta = 60, 70, 75, 80$. The
150 assimilated CO₂ fluxes deviated markedly from the “true” CO₂ fluxes when the
151 ensemble spread of $\lambda_{i,t}^a$ were too small for $\beta = 10, 50$ or when the ensemble spread
152 of $\lambda_{i,t}^a$ were too large for $\beta = 100$. Therefore, in this work, $\beta = 1.5$ was chosen to
153 make ensure the ensemble spread of $(\kappa_{i,t})_{\text{inf}}$ ranged from 0.1 to 1.25. Same as $\kappa_{i,t}$,
154 the ensemble mean values of $(\kappa_{i,t})_{\text{inf}}$ are 1. It is noted that perhaps there are very
155 few negative values for $(\kappa_{i,t})_{\text{inf}}$ after inflation. A quality control procedure is
156 performed for $(\kappa_{i,t})_{\text{inf}}$ before further appliance. All these negative data were set as
157 0.001 in this work. There was no special reason to set them as 0.001. It is also fine to
158 set them as 0. Then $(\kappa_{i,t})_{\text{inf}}$ were re-centered to ensure the ensemble mean values of
159 $(\kappa_{i,t})_{\text{inf}}$ were all 1.

160 As the concentrations were closely related to the emissions both locally and in
161 the upwind regions and there is no suitable dynamic model available to forecast the
162 emission scaling factors, the inflated concentration ratios $(\kappa_{i,t})_{\text{inf}}$ serve as the prior
163 emission scaling factors $\lambda_{i,t}^p$:

$$164 \quad \lambda_{i,t}^p = (\kappa_{i,t})_{\text{inf}}, (i = 1, \dots, N), (4)$$

165 The above equation is not supported according to the mass conservation equation
166 but just for the purpose to generate the ensemble emissions. Same as $(\kappa_{i,t})_{\text{inf}}$, $\lambda_{i,t}^p$
167 are numbers distributed around 1. From the perspective of generating the ensemble

168 emissions, they can play the same role as other data, such as the random numbers
 169 created by using the standard normal distribution function. However, there are
 170 correlations among the grid-points of $(\mathbf{\kappa}_{i,t})_{\text{inf}}$ because $(\mathbf{\kappa}_{i,t})_{\text{inf}}$ are calculated
 171 through a short-term forecast of WRF-Chem. Thus, $\lambda_{i,t}^{\text{p}}$ have the same correlations
 172 as $(\mathbf{\kappa}_{i,t})_{\text{inf}}$. While, the random numbers are totally different. There are no
 173 correlations unless they are generated under certain correlations.

174 To incorporate the useful information from the previous times, the previous DA
 175 cycles' analysis scaling factors, $\lambda_{i,t-M+1}^{\text{a}}, \dots, \lambda_{i,t-2}^{\text{a}}, \lambda_{i,t-1}^{\text{a}}$ and the prior scaling
 176 factor $\lambda_{i,t}^{\text{p}}$ were used to estimate $\lambda_{i,t}^{\text{f}}$ by the time smooth operator; namely,

$$177 \lambda_{i,t}^{\text{f}} = \frac{1}{M} \left(\sum_{j=t-M+1}^{t-1} \lambda_{i,j}^{\text{a}} + \lambda_{i,t}^{\text{p}} \right), (i = 1, \dots, N, j = t - M + 1, \dots, t - 1), (5)$$

178 Here, M is the time window of the smooth operator. In this study, a value of $M = 4$
 179 (hours) was chosen. According to the smooth operator, the ensemble mean values of
 180 $\lambda_{i,t}^{\text{f}}$ depend on the ensemble mean of $\lambda_{i,t-M+1}^{\text{a}}, \dots, \lambda_{i,t-2}^{\text{a}}, \lambda_{i,t-1}^{\text{a}}, \lambda_{i,t}^{\text{p}}$, where the
 181 ensemble means of $\lambda_{i,t}^{\text{p}}$ are all 1. After multiple iterations, the smooth operator can
 182 give comparatively good estimation for $\lambda_{i,t}^{\text{f}}$ since anthropogenic emissions are stable
 183 at a certain time scale (Mijling et al., 2012). It is a compromise between prescribed
 184 prior emissions and letting the system propagate all observation information from one
 185 step to the next without any guidance (Peters et al., 2007), for the case $M = 4$.

186 The ensemble members of the emissions were calculated according to

$$187 \mathbf{E}_{i,t} = \lambda_{i,t} \mathbf{E}_t^{\text{p}}, (i = 1, \dots, N), (6)$$

188 where $\mathbf{E}_{i,t}$ is the i th ensemble member of the emissions for each grid at time t , $\lambda_{i,t}$
 189 represents the scaling factors and \mathbf{E}_t^{p} is the prescribed emission, which can be
 190 obtained from the emission inventories. It is noted that the correlations among the
 191 grid-points of the prior emissions depend on $\lambda_{i,t}^{\text{p}}$. These correlations may deviate far
 192 from the truth but we have no other suitable substitute. However, the correlations
 193 among the grid-points of the forecast emissions should be more or less close to the
 194 truth due to the appliance of the smooth operator after multiple iterations.

195 It is noted although the method is very similar to that used by Peters et al. (2007)
196 and Peng et al. (2015) for CO₂ emission inversion, it is still of novelty for applications
197 in aerosol anthropogenic emissions. In Peters et al. (2007), $\lambda_{i,t}^p$ were all 1. And only
198 natural CO₂ emissions (i.e., biospheric and oceanic emissions) were assimilated at the
199 ecological scale due to the ‘signal-to-noise’ problem. Thus, the uncertainty of
200 anthropogenic and other CO₂ emissions were ignored. Besides, the framework is more
201 advanced compared to our previous work. In Peng et al. (2015), in order to generate
202 $\lambda_{i,t}^p$, a set of ensemble forecasts were performed from time t to $t+1$ to produce the CO₂
203 concentration fields, forced by the prescribed net CO₂ surface fluxes with the previous
204 assimilated concentration fields as initial conditions. That means that the ensemble
205 forecast were performed twice in that DA system and it was time consuming.
206 However, in order to save computing time, we used the chemical fields $C_{i,t}^f$ available
207 in the previous assimilation cycle to calculate $\lambda_{i,t}^p$ in this work. Thus, WRF-Chem
208 runs to forecast only once during a DA cycle.

209

210 **2.2 Ensemble square root filter**

211 The ensemble square root filter (EnSRF) algorithm was introduced by Whitaker
212 and Hamill (2002) and its expansion to analyzing aerosol ICs was described by
213 Schwartz et al. (2014). The traditional EnKF with perturbed observations (Evensen
214 1994) introduces sampling errors by perturbing the observations. In contrast to the
215 traditional EnKF, the EnSRF (Whitaker and Hamill, 2002) and the Ensemble
216 Adjustment Kalman Filter (EAKF, developed by Anderson, 2001) obviate the need to
217 perturb the observations. The local ensemble Kalman filtering (LEKF), a kind of
218 EnSRF, was presented by Ott et al. (2002, 2004). It was computationally more
219 efficient compared to the traditional EnKF, since it simultaneously assimilates the
220 observations within a spatially local volume independently. The local Ensemble
221 Transform Kalman Filter (LETKF, Hunt, 2007) integrates the advantages of the
222 Ensemble Transform Kalman Filter (ETKF, developed by Bishop et al., 2001) and the

223 LEKF. The computational cost of LETKF is much lower than that of the original
 224 LEKF because the former does not require an orthogonal basis. Though LETKF has
 225 more advantages, we still chose the same EnSRF as Schwartz et al. (2014) because we
 226 did not need to extend it to analyzing aerosol ICs, very similar to Schwartz et al.
 227 (2014).

228 Following the notation of Ide et al. (1997), given an m -dimensional background
 229 model forecast vector \mathbf{x}^b , a p -dimensional observation vector \mathbf{y}^o and an operator \mathbf{H}
 230 that converts the model state to the observation states, we expressed the variables as
 231 an ensemble mean (denoted by an over-bar) and a deviation from the mean (denoted
 232 by a prime). Thus, the ensemble mean $\bar{\mathbf{x}}^a$ of the analyzed state \mathbf{x}^a and the
 233 deviations \mathbf{x}'^a from the ensemble mean are updated separately by

$$234 \quad \bar{\mathbf{x}}^a = \bar{\mathbf{x}}^b + \mathbf{K}(\mathbf{y}^o - \mathbf{H}\bar{\mathbf{x}}^b), \quad (7)$$

$$235 \quad \mathbf{x}'^a = \mathbf{x}'^b + \tilde{\mathbf{K}}(\mathbf{y}'^o - \mathbf{H}\mathbf{x}'^b), \quad (8)$$

236 where \mathbf{K} is the traditional Kalman gain matrix and $\tilde{\mathbf{K}}$ is the gain used to update the
 237 deviations from the ensemble mean. These are given by

$$238 \quad \mathbf{K} = \mathbf{P}^b \mathbf{H}^T (\mathbf{H} \mathbf{P}^b \mathbf{H}^T + \mathbf{R})^{-1}, \quad (9)$$

$$239 \quad \begin{aligned} \tilde{\mathbf{K}} &= \mathbf{P}^b \mathbf{H}^T \left[\left(\sqrt{\mathbf{H} \mathbf{P}^b \mathbf{H}^T + \mathbf{R}} \right)^{-1} \right]^T \left(\sqrt{\mathbf{H} \mathbf{P}^b \mathbf{H}^T + \mathbf{R}} + \sqrt{\mathbf{R}} \right)^{-1} \\ &= \left(\mathbf{1} + \sqrt{\mathbf{R} / (\mathbf{H} \mathbf{P}^b \mathbf{H}^T + \mathbf{R})} \right)^{-1} \mathbf{K}, \quad (10) \end{aligned}$$

240 where $\mathbf{P}^b = \frac{1}{N-1} \sum_{i=1}^N \mathbf{x}'^b (\mathbf{x}'^b)^T$ is the $m * m$ -dimensional background error
 241 covariance matrix and \mathbf{R} is the $p * p$ -dimensional diagonal observation error
 242 covariance matrix. In real applications, $\mathbf{P}^b \mathbf{H}^T$ and $\mathbf{H} \mathbf{P}^b \mathbf{H}^T$ will be approximated
 243 using the background ensemble; namely,

$$244 \quad \mathbf{P}^b \mathbf{H}^T = \frac{1}{N-1} \sum_{i=1}^N \mathbf{x}'^b (\mathbf{H} \mathbf{x}'^b)^T \quad (11)$$

$$245 \quad \mathbf{H} \mathbf{P}^b \mathbf{H}^T = \frac{1}{N-1} \sum_{i=1}^N \mathbf{H} \mathbf{x}'^b (\mathbf{H} \mathbf{x}'^b)^T. \quad (12)$$

246 In equations (11) and (12), N is the ensemble size.

247 Note that for the joint analysis of ICs and emissions, the state vector \mathbf{x} is the
 248 joint vector of the mass concentration \mathbf{C} and the emission scaling factor $\boldsymbol{\lambda}$, i.e.
 249 $\mathbf{x} = [\mathbf{C}, \boldsymbol{\lambda}]^T$. In this study, the state variables of the analysis of the ICs were the 15

250 WRF-Chem/GOCART aerosol variables, same as that reported by Schwartz et al.
 251 (2012). The state variables of the emission scaling factors include $\lambda_{\text{PM}_{2.5}}$, λ_{SO_2} , λ_{NO}
 252 and λ_{NH_3} and are described in section 2.3.1. After each ensemble analysis, the
 253 ensemble forecasts were performed with the corresponding models to advance \mathbf{C} and
 254 λ to the next analysis time.

255 In this work, a 50-member ensemble was chosen, following Schwartz et al.
 256 (2012) and Whitaker and Hamill (2002). Covariance localization forced EnSRF
 257 analysis increments to zero 1280 km from an observation in the horizontal and one
 258 scale height to reduce spurious correlations due to sampling error for all control
 259 variables, similar to Pagowski et al., (2012) and Schwartz et al., (2012, 2014). In
 260 addition, posterior (after assimilation) multiplicative inflation following Whitaker and
 261 Hamill (2012) was applied aiming to maintain ensemble spread for only the
 262 concentration analysis. The inflation factor $\alpha = 1.2$ was chosen as Pagowski et al.,
 263 (2012) and Schwartz et al., (2012, 2014). Additive or prior inflation was not employed.
 264 As for the emission scaling factor λ , the inflation was not used at this step.

265

266 **2.3 Data assimilation system**

267 2.3.1 State variables

268 As stated in section. 2.2, the state variables of the analysis of the ICs were the 15
 269 WRF-Chem/GOCART aerosol variables. The $\text{PM}_{2.5}$ observation operator was the
 270 same as that described by Schwartz et al. (2012) and expressed as

$$271 \mathbf{y}^f = \rho_d [\mathbf{P}_{25} + 1.375\mathbf{S} + 1.8(\mathbf{OC}_1 + \mathbf{OC}_2) + \mathbf{BC}_1 + \mathbf{BC}_2 \\
 + \mathbf{D}_1 + 0.286\mathbf{D}_2 + \mathbf{S}_1 + 0.942\mathbf{S}_2], \quad (13)$$

272 where ρ_d represents the dry air density, which is multiplied by the mixing ratios of
 273 aerosol species (in $\mu\text{g}\cdot\text{kg}^{-1}$) to convert the units to $\mu\text{g m}^{-3}$ for consistency with the
 274 observations.

275 From the perspective of the optimization of emissions, four species of emission
 276 scaling factors ($\lambda_{\text{PM}_{2.5}}$, λ_{SO_2} , λ_{NO} and λ_{NH_3}) were also considered as the state
 277 variables of the DA system. Atmospheric inorganic aerosols are not only from the
 278 primary emissions, but also from secondary processes- chemical and thermodynamic

279 transformations from the gas-phase precursors. Therefore, not only the primary
 280 sources of PM_{2.5}, but also the sources of the gas-phase precursors, need to be
 281 optimized. In this study, the sources of SO₂, NO_x and NH₃ (\mathbf{E}_{SO_2} , \mathbf{E}_{NO} and \mathbf{E}_{NH_3}),
 282 which have a large impact on the distribution of PM_{2.5}, were also optimized in
 283 addition to the primary sources of PM_{2.5}. It is noted that for the optimization of the
 284 emission scaling factors, \mathbf{M}_{SF} serves as the forecast model and the observation
 285 operator reflects the combined information of emissions (in the format of $\boldsymbol{\lambda}$ in
 286 equation (6)), the physics and chemistry processes in WRF-Chem simulations and the
 287 transformation PM_{2.5} from model space to observation space (equation (13)).

288 The direct sources of PM_{2.5} include the unspiciated primary sources of PM_{2.5}
 289 $\mathbf{E}_{\text{PM}_{2.5}}$, sulfate \mathbf{E}_{SO_4} , nitrate \mathbf{E}_{NO_3} , organic compounds \mathbf{E}_{org} and elemental
 290 compounds \mathbf{E}_{BC} ; all of them are given in two modes (the nuclei and accumulation
 291 modes, represented as *i* and *j* in the subscripts respectively). The ratios between the
 292 nuclei and accumulation modes were the same as in the suggested emission process
 293 for National Emission Inventory in WRF-Chem (Freitas et al., 2011). The formula of
 294 sulfate and nitrate emissions in the model are as below:

$$295 \quad \mathbf{E}_{\text{PM}_{2.5i}} : \mathbf{E}_{\text{PM}_{2.5j}} = 1 : 4, (14)$$

$$296 \quad \mathbf{E}_{\text{SO}_{4i}} : \mathbf{E}_{\text{SO}_{4j}} = 1 : 4, (15)$$

$$297 \quad \mathbf{E}_{\text{NO}_{3i}} : \mathbf{E}_{\text{NO}_{3j}} = 1 : 4, (16)$$

$$298 \quad \mathbf{E}_{\text{SO}_{4i}} + \mathbf{E}_{\text{SO}_{4j}} = a * (\mathbf{E}_{\text{PM}_{2.5i}} + \mathbf{E}_{\text{PM}_{2.5j}} - \mathbf{E}_{\text{EC}} - \mathbf{E}_{\text{ORG}}), (17)$$

$$299 \quad \mathbf{E}_{\text{NO}_{3i}} + \mathbf{E}_{\text{NO}_{3j}} = b * (\mathbf{E}_{\text{PM}_{2.5i}} + \mathbf{E}_{\text{PM}_{2.5j}} - \mathbf{E}_{\text{EC}} - \mathbf{E}_{\text{ORG}}), (18)$$

300 where \mathbf{E}_{EC} represents elemental carbon and \mathbf{E}_{ORG} organic compounds, and
 301 $a = 0.074$ and $b = 0.038$ were chosen based on the internal emissions and
 302 observational data. In the DA process, the first 6 species of direct sources of
 303 emissions ($\mathbf{E}_{\text{PM}_{2.5i}}$, $\mathbf{E}_{\text{PM}_{2.5j}}$, $\mathbf{E}_{\text{SO}_{4i}}$, $\mathbf{E}_{\text{SO}_{4j}}$, $\mathbf{E}_{\text{NO}_{3i}}$, and $\mathbf{E}_{\text{NO}_{3j}}$), which may have
 304 larger uncertainties in heavy polluted events, were updated according to the variation
 305 of $\boldsymbol{\lambda}_{\text{PM}_{2.5}}$. $\mathbf{E}_{\text{PM}_{2.5i}}$ and $\mathbf{E}_{\text{PM}_{2.5j}}$ were directly updated according to the variation in
 306 $\boldsymbol{\lambda}_{\text{PM}_{2.5}}$. The emissions ($\mathbf{E}_{\text{SO}_{4i}}$, $\mathbf{E}_{\text{SO}_{4j}}$, $\mathbf{E}_{\text{NO}_{3i}}$ and $\mathbf{E}_{\text{NO}_{3j}}$) were also updated according
 307 to the variations in $\mathbf{E}_{\text{PM}_{2.5i}}$ and $\mathbf{E}_{\text{PM}_{2.5j}}$.

308 \mathbf{E}_{EC} and \mathbf{E}_{ORG} of the anthropogenic emissions were not assimilated, which is a
309 limitation in this work. Besides, emissions of dust and sea salt were not assimilated. It
310 is true that these emissions are also important for the atmosphere aerosol. The reason
311 we did not assimilate \mathbf{E}_{EC} and \mathbf{E}_{ORG} is that only the $\text{PM}_{2.5}$ measurements are used in
312 this DA experiment. However, the sources of the aerosols (especially organic aerosols)
313 are so complex that our knowledge of their formation mechanisms is far from clear.
314 Though it is technically possible to have all emissions assimilated, with such limited
315 observations adding more control variables would cause much more uncertainties in
316 the system which might lead to unreasonable analysis.

317

318 2.3.2 Procedure for the DA system

319 Figure 2 (b) shows the workflow of the DA system. The steps in this workflow are as
320 follows.

321 (1) The persistence forecasting operator \mathbf{M}_{SF} is applied to forecast the
322 background fields of the emission scaling factors $\lambda_{\text{PM}_{2.5}}^f$, $\lambda_{\text{SO}_2}^f$, λ_{NO}^f and $\lambda_{\text{NH}_3}^f$. The
323 forecast chemical fields of P_{25} , SO_2 , NO and NH_3 of the previous assimilation cycle
324 are used to create the prior emission scaling factors $\lambda_{\text{PM}_{2.5}}^p$, $\lambda_{\text{SO}_2}^p$, λ_{NO}^p and $\lambda_{\text{NH}_3}^p$.
325 The background scaling factors are then generated using equation (5).

326 (2) The ensemble members of the emissions, $\mathbf{E}_{\text{PM}_{2.5i}}^f$, $\mathbf{E}_{\text{PM}_{2.5j}}^f$, $\mathbf{E}_{\text{SO}_2}^f$, \mathbf{E}_{NO}^f and
327 $\mathbf{E}_{\text{NH}_3}^f$, are prepared according to equation (6). The corresponding emissions of $\mathbf{E}_{\text{SO}_4i}^f$,
328 $\mathbf{E}_{\text{SO}_4j}^f$, $\mathbf{E}_{\text{NO}_3i}^f$ and $\mathbf{E}_{\text{NO}_3j}^f$ are obtained based on equations (15–18). Other inorganic
329 species of the anthropogenic emission, such as \mathbf{E}_{EC} and \mathbf{E}_{ORG} , are not perturbed for
330 WRF-Chem. However, other anthropogenic emissions, such as $\mathbf{E}_{\text{PM}_{2.5}}$, \mathbf{E}_{SO_4} and
331 \mathbf{E}_{NO_3} , are much larger than \mathbf{E}_{EC} and \mathbf{E}_{ORG} in most area of China, and the ensemble
332 spreads of the aerosol concentrate largely dependent on the uncertainties of those
333 anthropogenic emissions. Besides, model errors raised from the meteorology, the
334 emission and the chemical model itself are compensated to some extent through the
335 use of multiplicative inflation. In other words, the ensemble spread of the
336 concentrations can be kept at a certain level though \mathbf{E}_{EC} and \mathbf{E}_{ORG} , are not

337 perturbed.

338 Natural emissions, such as dust and sea salt emissions were not perturbed
339 explicitly when the forecast emissions were generated. However, emissions of dust
340 and sea salt were parameterized within the GOCART model (Chin et al., 2002).
341 Within the DA system, varying meteorology across the members implicitly perturbed
342 dust and sea salt emissions.

343 (3) Forced by the changed emissions ($\mathbf{E}_{\text{PM}_{2.5i}}$, $\mathbf{E}_{\text{PM}_{2.5j}}$, \mathbf{E}_{SO_2} , \mathbf{E}_{NO} , \mathbf{E}_{NH_3} ,
344 $\mathbf{E}_{\text{SO}_{4i}}$, $\mathbf{E}_{\text{SO}_{4j}}$, $\mathbf{E}_{\text{NO}_{3i}}$ and $\mathbf{E}_{\text{NO}_{3j}}$ were substituted by $\mathbf{E}_{\text{PM}_{2.5i}}^f$, $\mathbf{E}_{\text{PM}_{2.5j}}^f$, $\mathbf{E}_{\text{SO}_2}^f$, \mathbf{E}_{NO}^f ,
345 $\mathbf{E}_{\text{NH}_3}^f$, $\mathbf{E}_{\text{SO}_{4i}}^f$, $\mathbf{E}_{\text{SO}_{4j}}^f$, $\mathbf{E}_{\text{NO}_{3i}}^f$ and $\mathbf{E}_{\text{NO}_{3j}}^f$; the other emissions such as \mathbf{E}_{EC} and \mathbf{E}_{ORG}
346 remained unchanged), WRF-Chem is run again to forecast the chemical fields $\boldsymbol{\rho}^f$
347 with the updated chemical fields of the previous assimilation cycle as the ICs. The
348 state variables, i.e., 15 aerosol species and four scaling factors, are then prepared.

349 (4) The model-simulated $\text{PM}_{2.5}$ concentration at the observation space is then
350 calculated via equation (13). At this time, the state vector $\mathbf{x}^f = [\mathbf{C}^f, \boldsymbol{\lambda}^f]^T$ was
351 prepared.

352 (5) In the assimilation step, the state variables, the concentrations of 14 defined
353 aerosol species and a 15th unspiciated aerosol, and the four species of emission
354 scaling factors $\boldsymbol{\lambda}_{\text{PM}_{2.5}}^f$, $\boldsymbol{\lambda}_{\text{SO}_2}^f$, $\boldsymbol{\lambda}_{\text{NO}}^f$ and $\boldsymbol{\lambda}_{\text{NH}_3}^f$, were optimized through EnSRF.

355 (6) After the assimilation step, the optimized emissions ($\mathbf{E}_{\text{PM}_{2.5i}}^a$, $\mathbf{E}_{\text{PM}_{2.5j}}^a$, $\mathbf{E}_{\text{SO}_2}^a$,
356 \mathbf{E}_{NO}^a , $\mathbf{E}_{\text{NH}_3}^a$, $\mathbf{E}_{\text{SO}_{4i}}^a$, $\mathbf{E}_{\text{SO}_{4j}}^a$, $\mathbf{E}_{\text{NO}_{3i}}^a$ and $\mathbf{E}_{\text{NO}_{3j}}^a$) were calculated according to equations
357 (6, 15–18) using the optimized scaling factors ($\boldsymbol{\lambda}_{\text{PM}_{2.5}}^a$, $\boldsymbol{\lambda}_{\text{SO}_2}^a$, $\boldsymbol{\lambda}_{\text{NO}}^a$ and $\boldsymbol{\lambda}_{\text{NH}_3}^a$).

358

359 **3. $\text{PM}_{2.5}$ observation data and errors**

360 Hourly averaged surface $\text{PM}_{2.5}$ observations from the Ministry of Environmental
361 Protection of China were assimilated. There were altogether 906 national control
362 measurement sites over China. The $\text{PM}_{2.5}$ observation sites spanned most of central
363 and eastern China but were primarily located in urban and suburban areas. So it
364 always happened that there were more than one observation sites in certain city,

365 which were fall into the same model grid. Since we did not know the exact station
366 type, We randomly selected one observation site in a city for assimilation experiment
367 and one for verification purposes to ensure that there was at most one assimilated
368 measurements for one model grid. Altogether 77 stations were selected for the PM_{2.5}
369 assimilation experiment and another 77 independent stations were selected for
370 verification. Figure 1 shows the locations of 77 measurement sites used for the PM_{2.5}
371 assimilation experiment and 77 independent sites used for forecast verification.

372 The observation error covariance matrix \mathbf{R} in equation (9) includes
373 contributions from measurement and representation errors. Similar to the work of
374 Schwartz et al. (2012), the measurement error ε_0 is defined as $\varepsilon_0 = 1.5 + 0.0075 * \Pi_0$,
375 where Π_0 denotes the observational values for PM_{2.5} ($\mu\text{g m}^{-3}$). Thus, higher
376 PM_{2.5} values were associated with larger measurement errors. Following Elbern et al.
377 (2007) and Pagowski et al. (2010), Schwartz et al. (2012), the representativeness error
378 ε_r depends on the resolution of the model and the characteristics of the observation
379 locations and is calculated as $\varepsilon_r = r\varepsilon_0\sqrt{\Delta x/L}$, where r is an adjustable parameter
380 (here, $r = 0.5$), Δx is the grid spacing (here, 40.5 km), and L is the radius of
381 influence of an observation (here, L was set to 3 km following Elbern et al. (2007),
382 since we do not know the station type that used in this work). The total PM_{2.5} error (ε_t)
383 is defined as $\varepsilon_t = \sqrt{\varepsilon_0^2 + \varepsilon_r^2}$. The observation errors are assumed to be uncorrelated
384 so that \mathbf{R} is a diagonal matrix.

385 The PM_{2.5} observations were subject to quality control to ensure data reliability
386 before DA. Considering that China has had intense pollution events, PM_{2.5} values
387 larger than $800 \mu\text{g m}^{-3}$ were classified as unrealistic and were not assimilated;
388 observations with the ensemble mean of the first guess departure exceeding 100
389 $\mu\text{g m}^{-3}$ were also omitted, following Schwartz et al. (2012). The numbers of the
390 observations were about 17700. Among them 8 observations were discarded because
391 they were larger than $800 \mu\text{g m}^{-3}$ and 243 (around 1.5%) were discarded due to the
392 latter reasons.

393

394 **4. Experimental design**

395 Two parallel experiments were performed to evaluate the impact of PM_{2.5} DA on the
396 analyses and forecasts of aerosols over China: an assimilation experiment and a
397 control experiment. Both experiments used identical WRF-Chem settings and
398 physical parameterizations.

399

400 4.1 Spin-up ensemble forecast with perturbed Initial and boundary conditions

401 The initialization and spin-up procedures were identical to those reported by
402 Schwartz et al. (2014). The ICs and lateral boundary conditions (LBCs) for the
403 meteorological fields were provided by the National Centers for Environmental
404 Prediction Global Forecast System (GFS).

405 The initial meteorological fields were created at 0000 UTC 1 October 2014 by
406 interpolating the GFS analyses onto the model domain. The 50 ensemble members
407 were then generated by adding Gaussian random noise with a zero mean and static
408 background error covariances (Torn et al., 2006) to the temperature, water vapor,
409 velocity, geopotential height and dry surface pressure fields. The ICs of each member
410 were zero in the initial aerosol fields, representing clean conditions as described by
411 Liu et al. (2011).

412 The LBCs for the meteorological fields were then interpolated from the GFS
413 analyses from 0000 UTC 1 October 2014 to 0000 UTC 16 October 2014 and
414 perturbed similarly to the initial fields at 0000 UTC 1 October 2014. The aerosol
415 LBCs of each member for all experiments were idealized profiles embedded within
416 the WRF/Chem model.

417 Fifty-member emissions were created by adding random noise to the
418 anthropogenic emissions, same as reported by Schwartz et al. (2014),

$$\mathbf{E}_{ip}^*(\eta, t) = \mathbf{E}_p(\eta, t) + \mathbf{W}_{ip} \boldsymbol{\sigma}_p^E(\eta, t)$$

419 where $\mathbf{E}_{ip}^*(\eta, t)$ is the i th ensemble member for the p th emissions variable at the
420 η th grid point and the t th hour, \mathbf{E}_p is the unperturbed emissions. The term $\boldsymbol{\sigma}_p^E$ is

421 the standard deviation of all \mathbf{E}_p values and in the horizontally adjacent points of grid
 422 box η at and within 2 h of t . \mathbf{W} is a weight that was randomly drawn from a
 423 standard Gaussian distribution and varied for each ensemble member and variable but
 424 was spatially and temporally constant. No correlations between emissions variables
 425 were considered, which was a limitation of this approach. For possible negative
 426 perturbed emissions, they were set as $\mathbf{E}_{ip}^*(\eta, t) = 0.001 * \mathbf{E}_p(\eta, t)$. This will increase
 427 the prescribed emissions more or less. However, only very few data were negative. So,
 428 this influence can be negligible.

429 Before the first DA cycle, a 50-member ensemble of four-day WRF-Chem
 430 forecasts was performed from 0000 UTC 1 October to 2300 UTC 4 October 2014
 431 using the perturbed ICs at 0000 UTC 1 October 2014, the corresponding perturbed
 432 LBCs and the emissions. Then a 50-member ensemble aerosol forecasts at 0000 UTC
 433 5 October 2014 were produced.

434

435 4.2 Assimilation experiments

436 Two DA experiments were performed. One was the pure assimilation of chemical ICs
 437 (hereafter expC), the others was the joint adjustment of chemical ICs and source
 438 emissions (hereafter expJ). Both DA experiments had same settings except for the
 439 emissions. They were conducted from 0000 UTC 5 October 2014 to 0000 UTC 16
 440 October 2014. The assimilation cycle interval was 1 h.

441 In the first DA cycle in expJ, the first 50 ensemble chemical fields were drawn
 442 from the WRF-Chem ensemble forecasts valid at 0000 UTC 5 October 2014, as
 443 described in section 4.1. Using the ensemble aerosol forecasts, the prior emission
 444 scaling factors $\lambda_{i,t}^p$ at 2300 UTC 4 October 2014 were calculated. $\lambda_{i,t}^p$ were used
 445 directly as $\lambda_{i,t}^f$ for the first 5 assimilation cycles (after 5 assimilation cycles, the
 446 system has been initialized, all future scaling factors could be created using the
 447 persistence forecasting operator \mathbf{M}_{SF}). Then, the state vector $\mathbf{x}^f = [\mathbf{C}^f, \boldsymbol{\lambda}^f]^T$ was
 448 prepared. And after that, the DA cycle started.

449 In expC, the first chemical fields were also drawn from the WRF-Chem

450 ensemble forecasts valid at 0000 UTC 5 October 2014. Then, the state vector
451 $\mathbf{x}^f = [\mathbf{C}^f]^T$ was prepared and the DA cycle started.

452 At the WRF-Chem forecast step of the subsequent assimilation cycles for both
453 experiments, the ICs for the chemical variables of each member were drawn from the
454 updated chemical fields of the previous cycle. The aerosol LBCs of each member for
455 all experiments were idealized profiles embedded within the WRF/Chem model. As
456 for the meteorological ensemble fields, the LBCs were prepared in advance as
457 depicted in section 4.1; the ICs of each member of the meteorological fields were
458 drawn from the forecast meteorological fields of the previous cycle before
459 re-centering with the GFS analysis because we do not do meteorological analysis:

$$460 \quad \boldsymbol{\pi}_{i_{\text{new}}} = \boldsymbol{\pi}_i + (\boldsymbol{\pi}_{\text{GFS}} - \bar{\boldsymbol{\pi}}), \quad (18)$$

461 where $\boldsymbol{\pi}_i$ is the i th member of the forecast meteorological fields of the previous
462 cycle, $\bar{\boldsymbol{\pi}}$ is the ensemble mean of the forecast meteorological fields of the previous
463 cycle, $\boldsymbol{\pi}_{\text{GFS}}$ is the meteorological field interpolated from the GFS analyses and
464 $\boldsymbol{\pi}_{i_{\text{new}}}$ is the new meteorological field used as the IC in WRF-Chem in the next cycle.

465 As stated in the first paragraph in this section, the settings of expC were the same
466 as those in expJ except for the emissions. In expJ, the ensemble anthropogenic
467 emissions were generated by using emission scaling factors. While in expC, the
468 ensemble anthropogenic emissions were prepared by adding random noise, as stated
469 in 4.1.

470

471 4.3 Control experiment

472 The control experiment was conducted for the same period as the assimilation
473 experiment and the simulation cycle period was 1 h, as in the assimilation experiment.
474 The first initial chemical fields were extracted from the ensemble mean valid at 0000
475 UTC 5 October 2014. In the subsequent simulation process, the ICs for the chemical
476 fields were from the previous cycle's 1-h forecast. The LBCs and ICs for the
477 meteorological fields were updated by interpolating the GFS analyses. The emissions
478 were the prescribed emissions \mathbf{E}_t^p without any perturbation.

479

480 **5. Results**

481 Statistics for both expJ and expC were computed using the ensemble mean prior
482 (background) and posterior (analysis) fields (average of the 50-member ensemble).
483 The ensemble performances were first examined. Output from the first day of the
484 cycling DA configurations was excluded from all verification statistics to allow the
485 ensemble fields to “spin up” from the initial ensemble.

486 As the measurement coverage is an important factor that may determine the
487 performance in DA, we primarily focused our attention on the results from three
488 sub-regions with comparatively dense observational coverage (Figure 1): the Beijing–
489 Tianjin–Hebei region (JJJ, 12 stations for assimilation and 12 stations for verification);
490 the Yangtze River delta (YRD, 24 stations for assimilation and 24 stations for
491 verification); and the Pearl River delta (PRD, 9 stations for assimilation and 9 stations
492 for verification).

493

494 5.1 Ensemble performance

495 It is important to assess the ensemble performance for an ensemble-based DA system.
496 In a well-calibrated system, a comparison of the prior ensemble mean
497 root-mean-square error (RMSE) with respect to the observations should equal the
498 prior “total spread” (square root of the sum of ensemble variance and observation
499 error variance) (Houtekamer et al., 2005). Figure 3 shows the time series for the prior
500 ensemble mean RMSE and the total spread for PM_{2.5} aggregated over all observations
501 in the three sub-regions for expJ. It indicates that the magnitudes of both the total
502 spread and the RMSE were influenced by the diurnal cycle and heavy air pollution.
503 Almost all the total spreads were smaller than the RMSE, showing an insufficient
504 spread of PM_{2.5} ensemble forecasts, which is especially evident for heavy polluted
505 period with much larger RMSEs. For expC, the characteristics of the prior ensemble
506 mean RMSE and the total spread for PM_{2.5} were very similar to that for the joint DA
507 experiment.

508 The magnitudes of the ensemble spread of the emission scaling factors of the

509 joint DA experiment were important for emission inversion. They were very stable
510 throughout the ~10 day experiment period, which indicates that \mathbf{M}_{SF} can generate
511 stable artificial data to generate the ensemble emissions. For $\lambda_{\text{PM}_{2.5}}^f$, they ranged
512 from 0.25 to 1 in most model area. Figure 3d shows the area-averaged time series
513 extracted from the ensemble spread of $\lambda_{\text{PM}_{2.5}}^f$. It shows that the ensemble spread was
514 stably distributed around 0.5, which indicates that the uncertainty of the ensemble
515 emissions was about 50%.

516

517 5.2 Impact on aerosol ICs

518 To evaluate quantitatively the impact of the ensemble assimilation system on the ICs,
519 the mean errors (bias), RMSEs and correlation coefficient (CORR) of the assimilation
520 experiment and the control run were first analyzed. These statistics were calculated
521 against independent observations over all the analyses from 6 to 16 October 2014.
522 Table 1 shows that the bias magnitudes of the control run were 15.9 and 20.6 $\mu\text{g m}^{-3}$
523 for the YRD and the PRD, respectively, suggesting a significant overestimation of the
524 WRF-Chem aerosol mass in these two sub-regions. However, a significant
525 underestimation of the aerosol mass occurred in the JJJ region, where the model bias
526 was $-18.0 \mu\text{g m}^{-3}$. The RMSEs of the control run were 81.6, 30.6 and 31.8 $\mu\text{g m}^{-3}$ for
527 the JJJ, YRD and PRD regions, respectively. After assimilation, the statistics showed
528 an apparent improvement and the magnitude of the bias and the RMSE decreased for
529 both DA experiment. For expJ, both the maximum bias and the RMSE were obtained
530 in the JJJ region, and were -10.3 and $66.9 \mu\text{g m}^{-3}$, respectively. The CORR increased
531 from 0.79, 0.60, and 0.62 to 0.83, 0.85, and 0.80 for the JJJ, YRD and PRD,
532 respectively. The statistics of expC were very similar to those of expJ. The bias and
533 the RMSE in the JJJ region were -12.2 and $64.0 \mu\text{g m}^{-3}$, respectively. And the CORR
534 were 0.85, 0.80, and 0.80 for the JJJ, YRD and PRD, respectively. These results
535 indicate that the initial $\text{PM}_{2.5}$ fields can be adjusted efficiently by the EnSRF.

536 It is interesting to note that expC has better RMSE and CORR than expJ but poor
537 bias in JJJ. And expC has better bias and RMSE than expJ but poor CORR in PRD.
538 Maybe small number of samples caused the uncertainties of the statics. However, the

539 differences were very small. The analysis of both experiments were very similar.

540 Then the analysis increments (i.e. $\bar{\mathbf{x}}^a - \bar{\mathbf{x}}^b$) were investigated to show the direct
541 impact of PM_{2.5} DA. They are determined by both the observation increments and the
542 relative magnitudes of the forecast error and the observation error, based on Equation
543 (7). From Figure 4(a), (e) and (f), the increments of both assimilation experiments
544 were distributed around the observations as expected. However, the impact of
545 assimilating PM_{2.5} observations was not limited to the areas where observations were
546 located, observations information was also transported to other areas through the
547 WRF-Chem forecast. Besides, the ensemble forecasts also partly contributed to the
548 spatial distribution of the PM_{2.5} mass. Therefore, the spatial distributions of the PM_{2.5}
549 mass in both assimilation experiments were significantly different from the control
550 run (see Figure 4(b), (c) and(d)), which suggest that assimilation PM_{2.5} observations
551 impacts greatly on the aerosol ICs. The PM_{2.5} mass magnitude of both assimilation
552 experiments were smaller than that of the control run at the lowest model level in the
553 YRD, the PRD and in central China. Conversely, positive differences (analysis minus
554 control) were gained in the JJJ region and in northeast China. These indicated the
555 reduction of the overestimation or underestimation of the WRF-Chem simulation over
556 these regions with data assimilation.

557

558 5.3 Impact on emissions

559 To determine the impact of assimilating PM_{2.5} observations on the chemical emissions,
560 we analyzed the area-averaged time series extracted from the forecast emission
561 scaling factors, the optimized emission scaling factors, the prior emissions and the
562 optimized emissions. Figure 5 shows that $\lambda_{\text{PM}_{2.5}}^f$ were changed along with $\lambda_{\text{PM}_{2.5}}^a$.
563 This indicates that observation information ingested from the previous observations
564 was incorporated through the usage of the time smooth operator.

565 Figure 5 also shows that although the prior emissions $\mathbf{E}_{\text{PM}_{2.5}}^p$ had no diurnal
566 variation when the experiments were designed, the optimized PM_{2.5} scaling factor,
567 $\lambda_{\text{PM}_{2.5}}^a$, showed an obvious variation with time, as did the optimized unspiciated

568 primary sources of $\text{PM}_{2.5}$, $\mathbf{E}_{\text{PM}_{2.5}}^{\text{a}}$. Moreover, the values of $\lambda_{\text{PM}_{2.5}}^{\text{a}}$ were <1 at almost
569 all times in the YRD and PRD, which resulted that the analyzed emission $\mathbf{E}_{\text{PM}_{2.5}}^{\text{a}}$
570 were lower than the prior $\text{PM}_{2.5}$ emissions $\mathbf{E}_{\text{PM}_{2.5}}^{\text{p}}$. In the YRD, the prior $\mathbf{E}_{\text{PM}_{2.5}}^{\text{p}}$ was
571 about $0.127 \mu\text{g m}^{-2} \text{s}^{-1}$ over all hours. After assimilation, the time-averaged optimized
572 $\mathbf{E}_{\text{PM}_{2.5}}^{\text{a}}$ decreased to $0.107 \mu\text{g m}^{-2} \text{s}^{-1}$, about 15.6% lower than the prior value. In the
573 PRD, the prior $\mathbf{E}_{\text{PM}_{2.5}}^{\text{p}}$ was about $0.10 \mu\text{g m}^{-2} \text{s}^{-1}$. The time-averaged optimized
574 $\mathbf{E}_{\text{PM}_{2.5}}^{\text{a}}$ decreased to $0.066 \mu\text{g}\cdot\text{m}^{-2} \text{s}^{-1}$, leading to a decrease of 35.0%. However,
575 larger values for the optimized $\mathbf{E}_{\text{PM}_{2.5}}^{\text{a}}$ were obtained in the JJJ region in three
576 periods, from 1600 UTC 6 October to 0000 UTC 8 October, from 1600 UTC 9
577 October to 0000 UTC 10 October, and from 1600 UTC 13 October to 0000 UTC 15
578 October as a result of the increased optimized scaling factor $\lambda_{\text{PM}_{2.5}}^{\text{a}}$. This may have
579 been caused by the burning of crop residues during harvesting in this region (Li et al.,
580 2016), which was not taken into account in the prior emissions. However, the $\text{PM}_{2.5}$
581 measurements network was still spatially sparse and heterogeneous in this work.
582 Almost all measurements were located in the city and no data available in the rural.
583 Meanwhile, the crop residues burning always occur in the rural region. Therefore, the
584 $\text{PM}_{2.5}$ measurements network can only capture the burning information a few hours
585 later. Hence, although the system is able to detect the emission changes caused by
586 burning events, the time that the system started to show increased scaling factors
587 might be not accurate enough (may shift a few hours later). Maybe a Kalman
588 smoother would have been a better system to solve this problem.

589 The NO , SO_2 and NH_3 emissions were all adjusted to some extent by our DA
590 approach (see Figure 6). The NO emissions increased by 41.3, 43.7 and 20.3% in the
591 JJJ, YRD and PRD regions, respectively. The SO_2 emissions increased by 16.3, 10.0
592 and 18.3% and the NH_3 emissions increased by 16.7, 7.8 and 7.5% in the JJJ, YRD
593 and PRD regions, respectively.

594 Figure 7 shows the spatial distribution of the time-averaged scaling factors
595 $\lambda_{\text{PM}_{2.5}}^{\text{a}}$ at the lowest model level over all hours from 6 to 16 October 2014, since the
596 emissions at higher levels were so small that the impact of assimilating $\text{PM}_{2.5}$

597 observations was negligible. Figure 8 shows the distribution of $E_{PM_{2.5}}^p$ and the
598 time-averaged differences between the ensemble mean of the assimilation and the
599 prior values.

600 These patterns are consistent with those in Figure 5. Negative differences were
601 obtained in most areas of the YRD and PRD, indicating that the $PM_{2.5}$ DA primarily
602 decreased the $PM_{2.5}$ emissions. Conversely, positive differences were obtained in
603 South Hebei, North Henan and Southeast Shanxi provinces, indicating that DA
604 increased the $PM_{2.5}$ emissions.

605 As the economy in China has developed, the spatiotemporal distribution of
606 emissions has changed as a result of changes in energy consumption, the structure of
607 the energy market and advances in technology. Therefore although this inventory of
608 emissions may have correctly described anthropogenic emissions in 2006 when it was
609 constructed, it is not representative of the anthropogenic emissions in 2014.
610 Theoretically, the assimilated emissions should reduce the uncertainty in the prior
611 emissions as a result of the application of observations. Different from the situations
612 that standard national emission inventories were reported by government in USA,
613 European or other countries, the rapid economic development and complexity of
614 emission sources in China lead to large uncertainties in the current emission
615 inventories even for the latest version. Thus it's impossible for us to conduct the
616 direct evaluation on emissions.

617 Although we had no direct emission observations to evaluate the analyzing
618 emissions, which was a challenging to many emission inversion research teams (e.g.
619 Tang et al, 2011; Miyazaki et al., 2012; Ding et al., 2015; Mclinden et al., 2016; etc.),
620 the improvement of emissions can be verified in terms of two aspect, the diurnal
621 variation and the location of increased emissions. The diurnal variation in the
622 assimilated emissions verified this statement to some extent. Especially in the PRD
623 and YRD, $E_{PM_{2.5}}^a$ in the daytime were always larger than those in the night, which
624 agreed well with Olivier et al. (2003), the WRAP (2006) and Wang et al. (2010). In
625 addition, the locations of the larger values for the optimized $E_{PM_{2.5}}^a$ in the JJJ region

626 was in good agreement with the place of the crop residues burning traced by the
627 environmental satellite of China. There were 10, 231, 37 and 3
628 crop residue burning spots in Hebei, Henan, Shandong and Shanxi province
629 respectively from 5 to 11 October 2014 and 7, 20, 5 and 21 respectively from 12 to 18
630 October 2014 (Weekly Crop Residue Burning Monitoring Report traced by
631 Environmental Satellite, 2015a, 2015b).

632 However, the analysis emissions are only a mathematical optimum. They are
633 influenced greatly by the model errors and the observation errors. In addition, only
634 surface $PM_{2.5}$ observations were applied in this work, which may lack abundant
635 constraint on the sources of the secondary aerosol precursors. More observations are
636 needed to obtain reliable emissions for the sources of the gas-phase precursors.

637

638 5.4 Verification of aerosol forecasting

639 For the assimilation experiment, 48-h forecasts were performed at each 0000
640 UTC from 6 to 16 October 2014 with the hourly forecast output for both assimilation
641 experiments. For the verification forecasting experiment for expJ (hereafter fcJ), the
642 ensemble mean of the analyzed ICs and emissions of expJ were used in this
643 longer-range model forecast. For the verification forecasting experiment for expC
644 (hereafter fcC), the ensemble mean of the analyzed ICs of expC and the prescribed
645 anthropogenic emissions were used.

646 In order to get a more visualized picture of the impact of DA for both
647 assimilation experiments, time series of the hourly $PM_{2.5}$ extracted from the analysis
648 (AN), the control run (CT) and the hourly output of 48-h forecast (fc24 for the first
649 day forecast and fc48 for the second day forecast) were compared with the
650 observations (OBS) for three megacities Beijing, Shanghai and Guangzhou,
651 respectively (Figure 9). As expected, the time series of the analysis (also the
652 background) were consistent with the observations. The control run showed large
653 deviations from the observations, especially in Shanghai and Guangzhou. Benefit
654 from DA on both the first day and the second day forecasts can be clearly seen.

655 The bias and the RMSE of the surface $PM_{2.5}$ forecasts as a function of forecast

656 range was then calculated against the independent observations for the three
657 sub-regions (Figure 10). Both the bias and the RMSEs of the control run were
658 characterized by the diurnal cycle in the YRD and PRD. The largest errors were seen
659 at 2100 UTC in the YRD (about $29 \mu\text{g}\cdot\text{m}^{-3}$ for bias and $37 \mu\text{g}\cdot\text{m}^{-3}$ for RMSEs) and at
660 2300 UTC in the PRD (about $36 \mu\text{g}\cdot\text{m}^{-3}$ for bias and $41 \mu\text{g}\cdot\text{m}^{-3}$ for RMSEs), likely
661 indicating significant systematic forecast errors at these times. From 0300 to 0900
662 UTC, the bias (about $1 \mu\text{g}\cdot\text{m}^{-3}$ in the YRD and $-5 \mu\text{g}\cdot\text{m}^{-3}$ in the PRD) and the RMSE
663 values (about $14 \mu\text{g}\cdot\text{m}^{-3}$ in the YRD and $16 \mu\text{g}\cdot\text{m}^{-3}$ in the PRD) were much smaller
664 than at other times in both the YRD and PRD, showing that WRF-Chem performed
665 well during this period. However, in the JJJ region, the bias (about $-20 \mu\text{g}\cdot\text{m}^{-3}$) and
666 the RMSEs (about $50 \mu\text{g}\cdot\text{m}^{-3}$) were always large as a result of a heavy pollution event.
667 After assimilation, both the magnitude of the bias and the RMSEs decreased sharply.
668 Especially in in YRD and PRD, most bias ranged from -5 to $5 \mu\text{g}\cdot\text{m}^{-3}$ and most
669 RMSEs ranged from 11 to $14 \mu\text{g}\cdot\text{m}^{-3}$, further indicating that DA greatly affected the
670 ICs.

671 The improvements in the surface $\text{PM}_{2.5}$ forecasts by the joint adjustment of the
672 ICs and emissions were very large in the YRD and PRD for expJ. Large reduction of
673 the magnitude of the bias and the RMSEs due to assimilation can be seen for almost
674 the entire 48-h forecast range. From 10- to 23-h and from 34- to 47-h, in particular,
675 the relative reduction in RMSE was about 37.5%. However, the DA impact was much
676 smaller for 3- to 9-h forecast ranges, which are at daytime of the first day forecast. In
677 addition, the improvements were nearly negligible in PRD from 27- to 33-h, the
678 daytime of the second day forecast, suggesting that the benefit gained from adjusting
679 the ICs decreased progressively and eventually disappeared with model integration.
680 And the performance was actually deteriorated in YRD during the same time. One of
681 the possible reasons was that chemical model performed sufficiently well during
682 daytime when the boundary layer was unstable and therefore the further improvement
683 was more difficult. And there were always large errors during the night when the
684 boundary layer was stable, so that large improvements could be obtained. The other
685 possible reason can be attributed to the a priori constant emissions. The differences

686 between the optimized $PM_{2.5}$ emissions and the prior emissions were comparatively
687 small during the day, but the optimized $PM_{2.5}$ emissions were much smaller than the a
688 prior emissions during the night. So that the control run could performed worse during
689 the night and it could performed well during the day. Given the a priori variable
690 emissions provided, the control run will perform better during the night. Nevertheless,
691 attributed greatly to the large adjustment of chemical emissions, substantial
692 improvements were still achieved from 34- to 47- h. These results revealed that joint
693 adjustment of the ICs and emissions can improve surface $PM_{2.5}$ forecasts up to 48 h in
694 the YRD and PRD.

695 As for expC, it seemed that large improvements in the surface $PM_{2.5}$ forecasts
696 were gained through the adjustment of the ICs in PRD from 10- to 23-h and from 34-
697 to 47-h. Large reduction of the magnitude of the bias and the RMSEs due to
698 assimilation can be seen during this period. The relative reduction in RMSE ranged
699 from 25% to 37.5%. However, the forecasts deviated much from the observations for
700 3- to 9-h and 27- to 33-h forecast ranges. One of the reason may be that the
701 adjustment of the ICs decreased the analysis field too much on the whole since the
702 WRF-Chem forecast aerosol mass was systematically overestimated in PRD (see
703 Figure 4, Figure 9f and Figure 10e). While this aerosol mass overestimation might be
704 also due to the possibly overestimated emissions in some time periods (not all-day
705 long) which are not corrected in the simulation. So the over-adjusted ICs compensated
706 the unadjusted emissions in some period but also lead to the negative biases for the
707 periods when emission is not overestimated or underestimated. The other factor was
708 the diurnal variation. It is very clear that $PM_{2.5}$ mass gradually decreased with time
709 from 0000 UTC to 0008 UTC and then obtained the smallest value. After that it
710 increased with time from 0009 UTC to 0023 UTC obtained the largest value at about
711 0000 UTC. Both reasons led to the systematically underestimation of $PM_{2.5}$ mass of
712 fcC from 3- to 9-h and from 27- to 33-h, though maybe the aerosol ICs were very
713 close to the observations. Therefore, both the magnitude of the bias and the RMSEs of
714 the fcC were larger than those of the control run. In addition, $PM_{2.5}$ forecasts of the
715 fcC were benefit much from the diurnal variation and the adjustment of the ICs from

716 10- to 23-h and from 34- to 47-h. As a consequence, the magnitude of the
717 corresponding bias and the RMSEs of the fcC were smaller than those of the control
718 run. Similar statics characteristics were also gained in YRD. But the improvements
719 were comparatively small from 10- to 23-h and from 34- to 47-h. However, the
720 performance of fcJ was always better than that of the fcC for almost the entire 48-h
721 forecast range in the PRD and YRD. This could be attributed much to the emissions
722 since the ICs of both forecasts were very similar. In the forecast experiment of expC,
723 the emissions were the default monthly anthropogenic emissions. While in the
724 forecast experiment of expJ, the assimilated emissions were different much from the
725 default monthly anthropogenic emissions (see Figure 5 and 6). Also, there was diurnal
726 variation.

727 Both DA systems did not perform as well in the JJJ region as in the YRD and
728 RRD and relatively smaller improvements were achieved in the first 24-h forecast.
729 One possible reason for this result may be systematic errors due to chemistry
730 mechanism in WRF-Chem. The sources of the aerosols are so complex that our
731 knowledge of their formation mechanisms is far from clear and large uncertainties
732 still exist in the model simulations. Chemical transport models have a tendency to
733 underestimate PM concentrations, especially during episodes of heavy pollution
734 (Denby et al., 2007) due to some missing reactions (Wang et al., 2014; Zhang et al.,
735 2015, Zheng et al., 2015; Chen et al., 2016). Another reason can be attributed to the
736 forecast meteorological fields. There were still large uncertainties, especially when
737 boundary layer was stable and the wind speed was very small during episodes of
738 heavy pollution. As a result, a large bias may be obtained in forecasts of heavy
739 pollution given the ICs and emission inventories achieved from the joint assimilation.
740 Another reason may be the sparse coverage of measurements. There were only 12
741 sites in the JJJ region (Figure 1) and the measurement coverage was much sparser
742 than in the YRD or PRD.

743

744 **6. Summary and Discussion**

745 The EnSRF algorithm was extended to adjust the chemical ICs and the primary

746 and precursor emissions to improve forecasts for surface PM_{2.5}. This system was
747 applied to assimilate hourly surface PM_{2.5} measurements from 5 to 16 October 2014
748 over China. To evaluate the effectiveness of DA, 48-h forecasts were performed using
749 the optimized ICs and emissions, together with a control experiment without DA.
750 Besides, the experiment of pure assimilation chemical ICs and the corresponding 48-h
751 forecasts experiment were also performed for comparison. The results indicated that
752 the forecasts with the optimized ICs and emissions performed much better than the
753 control simulations. Large improvements were achieved for almost all the 48-h
754 forecasts, particularly in the YRD and PRD. However, relatively smaller
755 improvements were achieved in the first 24-h forecast in the JJJ region, which may be
756 attributed to the sparse measurement coverage and the deficiencies in the model
757 system for forecasting heavy pollution. Comparing to the forecasts with only the
758 optimized ICs, the forecasts with the joint adjustment were always much better for
759 almost all the forecasts in the PRD and YRD. However, In the JJJ region, they were
760 very similar.

761 There are still some limitations in this study. Firstly, we use the default monthly
762 anthropogenic emissions as the prior emissions and no time variation was added to
763 keep objective, since no resolution of temporal allocations at shorter but critical
764 (e.g., day-of-week, diurnal) scales is available. As shown in earlier work, the constant
765 emissions will worsen the chemical forecasts (de Meij et al., 2006; Wang et al, 2009).
766 For the joint DA system itself, it cannot benefit from the constant prior anthropogenic
767 emissions. But the normalized RMSE in Figure 10g decreased due to the poor
768 forecasts of control run. The control run will perform better when variable emissions
769 within the day are allowed, especially during the night. As a result, the relative
770 reduction in RMSE could not be so large during the night. Secondly, no correlations
771 between emissions variables were considered when perturbing the emissions, which
772 will lead to the reduction of the correlations between the variables. Thus, the chemical
773 forecast will deviate from the truth to some degree. Fortunately, the perturbed
774 emissions were only used in the initialization and spin-up experiment and expC.
775 Therefore, there were no impacts on expJ and the control run except for expC. Thirdly,

776 E_{EC} and E_{ORG} are not perturbed in expJ. However, as stated in Sect. 2.3.2, the
777 ensemble spread of OC_1 and OC_2 can be kept at a certain level. As a result, OC_1
778 and OC_2 changed much contributed to the $PM_{2.5}$ assimilation in expJ, which
779 suggests that the influence of not perturbing E_{EC} and E_{ORG} could be negligible. But,
780 because of the too small magnitudes of BC_1 and BC_2 , the differences (assimilation
781 minus control) of BC_1 and BC_2 were nearly close to zero. Fourthly, the experiment
782 (expE) where only emissions were assimilated was not included here. But it was still
783 worth to simultaneously assimilate the chemical ICs and emission. For one thing, in
784 expE, the chemical concentrations can be updated by the WRF-Chem model
785 simulations with the assimilated emissions as the initial field in each DA cycle. That
786 means that the 50-member ensemble forecasts were performed twice and it was time
787 consuming. For another, better concentration analysis could be obtained in expJ due
788 to the simultaneous assimilation of ICs and emissions. While in expE, there may be
789 larger uncertainties for the updated chemical concentrations through WRF-Chem due
790 to the deficiency of chemistries and the uncertainties of the ICs. This will lead to
791 larger uncertainties for the emission inversion. Also the improvement of $PM_{2.5}$
792 forecasts will be limited due to the comparatively poor chemical ICs.

793 This study represents the first step in the simultaneous optimization of chemical
794 ICs and emissions and only surface $PM_{2.5}$ measurements were assimilated. In future
795 work, gas-phase observations of SO_2 , NO_2 and CO will be used to further improve the
796 performance of this DA system.

797

798 References

- 799 Anderson, J.L.: An Ensemble Adjustment Kalman Filter for Data Assimilation,
800 Mon.Weather Rev., 129, 2884–2903, 2001.
- 801 Adhikary, B., Kulkarni, S., Dallura, A., Tang, Y., Chai, T., Leung, L. R., Qian, Y.,
802 Chung, C. E., Ramanathan, V., and Carmichael, G. R.: A regional scale chemical
803 transport modeling of Asian aerosols with data assimilation of AOD observations
804 using optimal interpolation technique, Atmos. Environ., 42, 8600–8615,
805 doi:10.1016/j.atmosenv.2008.08.031, 2008.
- 806 Barbu, A. L., Segers, A. J., Schaap, M., Heemink, A.W., and Builtjes, P. J. H.: A
807 multi-component data assimilation experiment directed to sulphur dioxide and
808 sulphate over Europe, Atmos. Environ., 43, 1622–1631, 2009.
- 809 Benedetti, A., Morcrette, J., Boucher, O., Dethof, A., Engelen, R., Fisher, M., Flentje,
810 H., Huneus, N., Jones, L., and Kaiser, J.: Aerosol analysis and forecast in the
811 European Centre for Medium-Range Weather Forecasts Integrated Forecast
812 System: 2. Data assimilation, J. Geophys. Res., 114, D13205,
813 doi:10.1029/2008JD011115, 2009.
- 814 Bishop, C. H., Etherton, B. J., and Majumdar, S. J.: Adaptive sampling with the
815 ensemble transform Kalman filter. Part I: Theoretical aspects, Mon. Weather
816 Rev., 129, 420–436, 2001.
- 817 Chen, D., Liu, Z., Fast, J., and Ban, J.: Simulations of Sulfate-Nitrate-Ammonium
818 (SNA) aerosols during the extreme haze events over Northern China in October
819 2014, Atmos. Chem. Phys. Discuss., doi:10.5194/acp-2016-222, in review, 2016.
- 820 Chin, M., Rood, R. B., Lin, S. J., Muller, J. F., and Thompson, A. M.: Atmospheric
821 sulfur cycle simulated in the global model GOCART: Model description and
822 global properties, J. Geophys. Res.-Atmos., 105, 24671–24687, 2000.
- 823 Chin, M., Ginoux, P., Kinne, S., Torres, O., Holben, B.N., Duncan, B. N., Martin,
824 R.V., Logan, J.A., Higurashi, A., and Nakajima, J.: Tropospheric aerosol optical
825 thickness from the GOCART model and comparisons with satellite and Sun
826 photometer measurements, J. Atmos. Sci., 59(3), 461–483, 2002.
- 827 Collins, W. D., Rasch, P. J., Eaton, B. E., Khattatov, B. V., and J.-F. Lamarque, J.-F.:

828 Simulating aerosols using a chemical transport model with assimilation of
829 satellite aerosol retrievals: Methodology for INDOEX, *J. Geophys. Res.*, 106,
830 7313–7336, 2001.

831 de Meij, A., Krol, M., Dentener, F., Vignati, E., Cuvelier, C., and Thunis, P.: The
832 sensitivity of aerosol in Europe to two different emission inventories and
833 temporal distribution of emissions, *Atmos. Chem. Phys.*, 6, 4287-4309,
834 doi:10.5194/acp-6-4287-2006, 2006.

835 Dai, T., Schutgens, N.A.J., Goto, D. Shi, G.Y., Nakajima, T.: Improvement of aerosol
836 optical properties modeling over Eastern Asia with MODIS AOD assimilation
837 in a global non-hydrostatic icosahedral aerosol transport model, *Environ. Pollut.*,
838 195, 319–329, 2014.

839 Denby, B., Schaap, M., Segers, A.J., Builtjes, P.J.H., Horalek, J.: Comparison of two
840 data assimilation methods for assessing PM10 exceedances on the European
841 scale, *Atmos. Environ.*, 42 (30), 7122–7134, 2007.

842 Ding, J., van der A, R. J., Mijling, B., Levelt, P. F., and Hao, N.: NO_x emission
843 estimates during the 2014 Youth Olympic Games in Nanjing, *Atmos. Chem.*
844 *Phys.*, 15, 9399-9412, doi:10.5194/acp-15-9399-2015, 2015.

845 Dubovik, O., Lapyonok, T., Kaufman, Y. J., Chin, M., Ginoux, P., Kahn, R. A., and
846 Sinyuk, A.: Retrieving global aerosol sources from satellites using inverse
847 modeling, *Atmos. Chem. Phys.*, 8, 209–250, doi:10.5194/acp-8-209-2008, 2008

848 Elbern, H., Strunk, A., Schmidt, H., and Talagrand, O.: Emission rate and chemical
849 state estimation by 4-dimensional variational inversion, *Atmos. Chem. Phys.*, 7,
850 3749–3769, doi:10.5194/acp-7-3749-2007, 2007.

851 Evensen, G.: Sequential data assimilation with a nonlinear quasi-geostrophic model
852 using Monte Carlo methods to forecast error statistics, *J. Geophys. Res.*, 99(C5),
853 10143–10162, 1994.

854 Freitas, S. R.; Longo, K. M.; Alonso, M. F.; Pirre, M.; Marecal, V.; Grell, G.;
855 Stockler, R.; Mello, R. F.; Sánchez Gácita, M.. PREP-CHEM-SRC 1.0: a
856 preprocessor of trace gas and aerosol emission fields for regional and global
857 atmospheric chemistry models. *Geoscientific Model Development*, v. 4, p.

858 419-433, 2011.

859 Ginoux, P., Chin, M. Tegen, I., Prospero, J. M., Holben, B., Dubovik, O., and Lin,
860 S.-J.: Sources and distributions of dust aerosols simulated with the GOCART
861 model, *J. Geophys. Res.*, 106, 20,255–20,273, doi:10.1029/2000JD000053,
862 2001.

863 Grell, G., Peckham, S. E., Schmitz, R., McKeen, S. A., Frost, G., Skamarock, W. C.,
864 and Eder, B.: Fully coupled “online” chemistry within the WRF model, *Atmos.*
865 *Environ.*, 39, 6957–6975, doi:10.1016/j.atmosenv.2005.04.027, 2005.

866 Guenther, A., Hewitt, C. N., Erickson, D., Fall, R., Geron, C., Graedel, T., Harley, P.,
867 Klinger, L., Lerdau, M., McKay, W., Pierce, T., Scholes, B., Steinbrecher, R.,
868 Tallamraju, R., Taylor, J., and Zimmerman, P.: A global model of natural
869 volatile organic compound emissions, *J. Geophys. Res.*, 100, 8873–8892,
870 doi:10.1029/94JD02950, 1995.

871 Guerrette, J. J. and Henze, D. K.: Development and application of the
872 WRFPLUS-Chem online chemistry adjoint and WRFDA-Chem assimilation
873 system, *Geosci. Model Dev.*, 8, 1857-1876, doi:10.5194/gmd-8-1857-2015,
874 2015.

875 Hakami, A., Henze, D. K., Seinfeld, J. H., Chai, T., Tang, Y., Carmichael, G. R., and
876 Sandu, A.: Adjoint inverse modeling of black carbon during the Asian Pacific
877 Regional Aerosol Characterization Experiment, *J. Geophys. Res.-Atmos.*, 110,
878 D14301, doi:10.1029/2004JD005671, 2005.

879 Heemink, A.W., and Segers, A.J.: Modeling and prediction of environmental data in
880 space and time using Kalman filtering, *Stoch. Environ. Res. Risk Assess.* 16 (3),
881 225–240, 2002.

882 Henze, D. K., Hakami, A., and Seinfeld, J. H.: Development of the adjoint of
883 GEOS-Chem, *Atmos. Chem. Phys.*, 7, 2413–2433, doi:10.5194/acp-7-2413-2007,
884 2007.

885 Henze, D. K., Seinfeld, J. H., and Shindell, D. T.: Inverse modeling and mapping US
886 air quality influences of inorganic PM_{2.5} precursor emissions using the adjoint
887 of GEOS-Chem, *Atmos. Chem. Phys.*, 9, 5877–5903,

888 doi:10.5194/acp-9-5877-2009, 2009.

889 Houtekamer, P. L., Mitchell, H. L., Pellerin, G., Buehner, M., Charron, M., Spacek, L.,
890 and Hansen, B.: Atmospheric data assimilation with an ensemble Kalman filter:
891 Results with real observations, *Mon. Weather Rev.*, 133, 604–620, 2005.

892 Ide, K., Courtier, P., Ghil, M., and Lorenc, A. C.: Unified notation for data
893 assimilation: operational, sequential and variational, *J. Meteorol. Soc. Japan*, 75,
894 181–189, 1997.

895 Jiang, Z., Liu, Z., Wang, T., Schwartz, C. S., Lin, H.-C., and Jiang, F.: Probing into
896 the impact of 3DVAR assimilation of surface PM10 observations over China
897 using process analysis, *J. Geophys. Res. Atmos.*, 118, 6738–6749,
898 doi:10.1002/jgrd.50495, 2013.

899 Peters, W., Jacobson, A. R., Sweeney, C., Andrews, A. E., Conway, T. J., Masarie, K.,
900 Miller, J. B., Bruhwiler, L. M. P., Petron, G., Hirsch, A. I., Worthy, D. E. J., van
901 der Werf, G. R., Randerson, J. T., Wennberg, P. O., Krol, M. C., Tans, P. P.: An
902 atmospheric perspective on North American carbon dioxide exchange:
903 CarbonTracker, *P. Natl. Acad. Sci. USA*, 104, 18925–18930, 2007.

904 Kahnert, M.: Variational data analysis of aerosol species in a regional CTM:
905 Background error covariance constraint and aerosol optical observation operators,
906 *Tellus, Ser. B*, 60, 753–770, doi:10.1111/j.1600-0889.2008.00377, 2008.

907 Kleist, D. T., Parrish, D. F., Derber, J. C., Treadon, R., Wu, W.-S., and Lord, S.:
908 Introduction of the GSI into the NCEP global data assimilation system, *Weather*
909 *Forecast.*, 24, 1691–1705, 2009.

910 Huneus, N., Chevallier, F., and Boucher, O.: Estimating aerosol emissions by
911 assimilating observed aerosol optical depth in a global aerosol model, *Atmos.*
912 *Chem. Phys.*, 12, 4585–4606, doi:10.5194/acp-12-4585-2012, 2012.

913 Huneus, N., Boucher, O., and Chevallier, F.: Atmospheric inversion of SO₂ and
914 primary aerosol emissions for the year 2010, *Atmos. Chem. Phys.*, 13,
915 6555–6573, doi:10.5194/acp-13-6555-2013, 2013.

916 Hunt, B., Kostelich, E., and Szunyogh, I.: Efficient data assimilation for
917 spatiotemporal chaos: a Local Ensemble Transform Kalman Filter, *Physica D*,

918 230, 112–126, 2007.

919 Lee, E.-H., Ha, J.-C., Lee, S.-S., and Chun, Y.: PM10 data assimilation over South
920 Korea to Asian dust forecasting model with the optimal interpolation method,
921 Asia-Pacific J. Atmos. Sci., 49(1), 73–85, doi:10.1007/s13143-013-0009-y,
922 2013.

923 Li, Z., Zang, Z., Li, Q. B., Chao, Y., Chen, D., Ye, Z., Liu, Y., and Liou, K. N.: A
924 three-dimensional variational data assimilation system for multiple aerosol
925 species with WRF/Chem and an application to PM_{2.5} prediction, Atmos. Chem.
926 Phys., 13, 4265-4278, doi:10.5194/acp-13-4265-2013, 2013.

927 Li, J., Li, Y., Bo, Y., and Xie, S.: High-resolution historical emission inventories of
928 crop residue burning in fields in China for the period 1990–2013, Atmos.
929 Environ., 138, 152–161, 2016.

930 Liu, Z., Liu, Q., Lin, H. C., Schwartz, C. S., Lee, Y. H., and Wang, T.:
931 Three-dimensional variational assimilation of MODIS aerosol optical depth:
932 implementation and application to a dust storm over East Asia, J. Geophys. Res.,
933 116, D23206, doi:10.1029/2011JD016159, 2011.

934 Liu, F., Zhang, Q., Tong, D., Zheng, B., Li, M., Huo, H., and He, K. B.:
935 High-resolution inventory of technologies, activities, and emissions of coal-fired
936 power plants in China from 1990 to 2010, Atmos. Chem. Phys., 15,
937 13299-13317, doi:10.5194/acp-15-13299-2015, 2015.

938 McLinden, C.A., Fioletov, V., Shephard, M.W., Krotkov, N., Li, C., Martin, R.V.,
939 Moran, M.D., and J. Joiner,: Space-based detection of missing sulfur dioxide
940 sources of global air pollution, Nat. Geosci., 9, 496–500, doi:10.1038/ngeo2724,
941 2016.

942 Mijling, B. and van der A, R. J.: Using daily satellite observations to estimate
943 emissions of short-lived air pollutants on a mesoscopic scale, J. Geophys. Res.,
944 117, D17302, doi:10.1029/2012JD017817, 2012.

945 Miyazaki, K., Eskes, H. J., Sudo, K., Takigawa, M., van Weele, M., and Boersma, K.
946 F.: Simultaneous assimilation of satellite NO₂, O₃, CO, and HNO₃ data for the
947 analysis of tropospheric chemical composition and emissions, Atmos. Chem.

948 Phys., 12, 9545– 9579, doi:10.5194/acp-12-9545-2012, 2012.

949 Miyazaki, K., Eskes, H. J., Sudo, K., and Zhang, C.: Global lightning NO_x production
950 estimated by an assimilation of multiple satellite data sets, *Atmos. Chem. Phys.*,
951 14, 3277–3305, doi:10.5194/acp-14-3277-2014, 2014.

952 Ott, E., Hunt, B. R., Szunyogh, I., Zimin, A. V., Kostelich, E. J., et al.: Exploiting
953 local low dimensionality of the atmospheric dynamics for efficient Kalman
954 filtering, arXiv:physics/0203058, 24 pp., available at:
955 <http://arxiv.org/abs/physics/0203058v3/>, 2002.

956 Ott, E., Hunt, B. R., Szunyogh, I., Zimin, A. V., Kostelich, E. J., et al.: A local
957 ensemble Kalman filter for atmospheric data assimilation, *Tellus A*, 56, 415–428,
958 2004.

959 Pagowski, M., Grell, G. A., McKeen, S. A., Peckham, S. E., and Devenyi, D.:
960 Three-dimensional variational data assimilation of ozone and fine particulate
961 matter observations: some results using the Weather Research and Forecasting –
962 Chemistry model and Grid-point Statistical Interpolation, *Q. J. Roy. Meteor. Soc.*,
963 136, 2013–2024, doi:10.1002/qj.700, 2010.

964 Pagowski, M., and Grell, G. A.: Experiments with the assimilation of fine aerosols
965 using an ensemble Kalman filter, *J. Geophys. Res.-Atmos.*, 117, D21302,
966 doi:10.1029/2012jd018333, 2012.

967 Peng, Z., Zhang, M., Kou, X., Tian, X., and Ma, X.: A regional carbon data
968 assimilation system and its preliminary evaluation in East Asia, *Atmos. Chem.*
969 *Phys.*, 15, 1087-1104, doi:10.5194/acp-15-1087-2015, 2015.

970 Pope, C. A.: Review: Epidemiological basis for particulate air pollution health
971 standards, *Aerosol Sci. Tech.*, 32, 4–14, 2000.

972 Pope, C. A., Burnett, R. T., Thun, M. J., Calle, E. E., Krewski, D., Ito, K., and
973 Thurston, G. D.: Lung cancer, cardiopulmonary mortality, and long-term
974 exposure to fine particulate air pollution, *J. Am. Med. Assoc.*, 287, 1132–1141,
975 2002.

976 Rubin, J. I., Reid, J. S., Hansen, J. A., Anderson, J. L., Collins, N., Hoar, T. J., Hogan,
977 T., Lynch, P., McLay, J., Reynolds, C. A., Sessions, W. R., Westphal, D. L., and

978 Zhang, J.: Development of the Ensemble Navy Aerosol Analysis Prediction
979 System (ENAAAPS) and its application of the Data Assimilation Research
980 Testbed (DART) in support of aerosol forecasting, *Atmos. Chem. Phys.*, 16,
981 3927-3951, doi:10.5194/acp-16-3927-2016, 2016.

982 Saide, P. E., Carmichael, G. R., Liu, Z., Schwartz, C. S., Lin, H. C., da Silva, A. M.,
983 and Hyer, E.: Aerosol optical depth assimilation for a size-resolved sectional
984 model: impacts of observationally constrained, multi-wavelength and fine mode
985 retrievals on regional scale analyses and forecasts, *Atmos. Chem. Phys.*, 13,
986 10425-10444, doi:10.5194/acp-13-10425-2013, 2013.

987 Schwartz, C. S., Liu, Z., Lin, H. C., and McKeen, S. A.: Simultaneous
988 three-dimensional variational assimilation of surface fine particulate matter and
989 MODIS aerosol optical depth, *J. Geophys. Res.*, 117, D13202,
990 doi:10.1029/2011JD017383, 2012.

991 Schwartz, C. S., Liu, Z., Lin, H.-C., and Cetola, J. D.: Assimilating aerosol
992 observations with a “hybrid” variational-ensemble data assimilation system, *J.*
993 *Geophys. Res. Atmos.*, 119, 4043–4069, doi:10.1002/2013JD020937, 2014.

994 Sekiyama, T. T., Tanaka, T. Y., Shimizu, A., and Miyoshi, T.: Data assimilation of
995 CALIPSO aerosol observations, *Atmos. Chem. Phys.*, 10, 39-49,
996 doi:10.5194/acp-10-39-2010, 2010.

997 Schutgens, N. A. J., Miyoshi, T., Takemura, T., and Nakajima, T.: Sensitivity tests for
998 an ensemble Kalman filter for aerosol assimilation, *Atmos. Chem. Phys.*, 10,
999 6583-6600, doi:10.5194/acp-10-6583-2010, 2010.

1000 Schutgens, N. A. J., Miyoshi, T., Takemura, T., and Nakajima, T.: Applying an
1001 ensemble Kalman filter to the assimilation of AERONET observations in a
1002 global aerosol transport model, *Atmos. Chem. Phys.*, 10, 2561-2576,
1003 doi:10.5194/acp-10-2561-2010, 2010.

1004 Schutgens, N., Nakata, M., and Nakajima, T.: Estimating Aerosol Emissions by
1005 Assimilating Remote Sensing Observations into a Global Transport Model,
1006 *Remote Sensing*, 4, 3528-3543, 2012.

1007 Tang, X., Zhu, J., Wang, Z. F., and Gbaguidi, A.: Improvement of ozone forecast over

1008 Beijing based on ensemble Kalman filter with simultaneous adjustment of initial
1009 conditions and emissions, *Atmos. Chem. Phys.*, 11, 12901–12916,
1010 doi:10.5194/acp-11-12901-2011, 2011.

1011 Tombette, M., Mallet, V., and Sportisse, B.: PM10 data assimilation over Europe with
1012 the optimal interpolation method, *Atmos. Chem. Phys.*, 9, 57-70,
1013 doi:10.5194/acp-9-57-2009, 2009.

1014 Torn, R. D., Hakim, G. J., and Snyder, C.: Boundary conditions for limited-area
1015 ensemble Kalman filters, *Mon. Weather Rev.*, 134, 2490–2502, 2006.

1016 van Loon, M., Builtjes, P. J. H., and Segers, A. J.: Data assimilation of ozone in the
1017 atmospheric transport chemistry model LOTOS, *Environ. Model. Softw.*, 15,
1018 603–609, 2000.

1019 Wang, J., Xu, X., Henze, D. K., Zeng, J., Ji, Q., Tsay, S.-C., and Huang, J.: Top-down
1020 estimate of dust emissions through integration of MODIS and MISR aerosol
1021 retrievals with the GEOS-Chem adjoint model, *Geophys. Res. Lett.*, 39, L08802,
1022 doi:10.1029/2012GL051136, 2012.

1023 Wang, Y. X., Zhang, Q. Q., Jiang, J. K., Zhou, W., Wang, B. Y., He, K. B., Duan, F.
1024 K., Zhang, Q., Philip, S., and Xie, Y. Y.: Enhanced sulfate formation during
1025 China's severe winter haze episode in January 2013 missing from current models,
1026 *J.Geophys.Res.-Atmos.*, 119, 10.1002/2013JD021426, 2014

1027 Wang, X.Y., Liang, X.Z., Jiang, W.M., Tao, Z.N., Wang, J.X.L., Liu, H.N., Han
1028 Z.W., Liu, S.Y., Zhang, Y.Y., Grell, G.A., Peckham, S.E.: WRF-Chem
1029 simulation of East Asian air quality: Sensitivity to temporal and vertical
1030 emissions distributions, *Atmospheric Environment*, 44(2010) 660-669

1031 Whitaker, J. S., and Hamill, T. M.: Ensemble data assimilation without perturbed
1032 observations, *Mon. Weather Rev.*, 130, 1913–1924, 2002.

1033 Woo, J.H., Baek, J.M., Kim, J.W., Carmichael, G.R., Thongboonchoo, N., Kim, S.T.,
1034 An, J.H.: Development of a Multi-Resolution Emission Inventory and Its Impact
1035 on Sulfur Distribution for Northeast Asia, *Water, Air, and Soil Pollution* 148:
1036 259–278, 2003.

1037 Weekly Crop Residue Burning Monitoring Report ,

1038 <http://hjj.mep.gov.cn/jgjs/201510/P020151012746205487305.pdf>, 2015a (in
1039 Chinese).

1040 Weekly Crop Residue Burning Monitoring Report,
1041 <http://hjj.mep.gov.cn/jgjs/201510/P020151019568921489639.pdf>, 2015b(in
1042 Chinese).

1043 Xia Y., Zhao, Y., Nielsen, C.P., Benefits of China's efforts in gaseous pollutant
1044 control indicated by the bottom-up emissions and satellite observations
1045 2000-2014, *Atmospheric Environment*, 136, 43-53, 2016

1046 Yu, H., Dickinson, R. E., Chin, M., Kaufman, Y. J., Geogdzhayev, B., and
1047 Mishchenko, M. I.: Annual cycle of global distributions of aerosol optical depth
1048 from integration of MODIS retrievals and GOCART model simulations, *J.*
1049 *Geophys. Res.*, 108(D3), 4128, doi:10.1029/2002JD002717, 2003.

1050 Yumimoto, K., Uno, I., Sugimoto, N., Shimizu, A., and Satake, S.: Adjoint inverse
1051 modeling of dust emission and transport over East Asia, *Geophys. Res. Lett.*, 34,
1052 L00806, doi:10.029/2006GL028551, 2007.

1053 Yumimoto, K., Uno, I., Sugimoto, N., Shimizu, A., Liu, Z., and Winker, D. M.:
1054 Adjoint inversion modeling of Asian dust emission using lidar observations,
1055 *Atmos. Chem. Phys.*, 8, 2869-2884, doi:10.5194/acp-8-2869-2008, 2008.

1056 Yumimoto, K., Nagao, T.M., Kikuchi, M., Sekiyama, T.T, Murakami, H.,Tanaka,
1057 T.Y., Ogi, A., Irie, H., Khatri, P., Okumura, H., Arai, K., Morino, I., Uchino, O.,
1058 Maki, T.: Aerosol data assimilation using data from Himawari-8, a
1059 next-generation geostationary meteorological satellite, *Geophys. Res. Lett.*, 43,
1060 5886–5894, 2016.

1061 Yin, X.M., Dai, T., Xin, J.Y., Gong, D.Y., Yang, J., Teruyuki, N., Shi, G.Y.:
1062 Estimation of aerosol properties over the Chinese desert region with MODIS
1063 AOD assimilation in a global model, *Adv. Clim. Change Res.*, 7, 90–98, 2016.

1064 Zhang, J., Reid, J. S., Westphal, D., Baker, N., and Hyer, E.: A System for
1065 Operational Aerosol Optical Depth Data Assimilation over Global Oceans, *J.*
1066 *Geophys. Res.*, 113, D10208, doi:10.1029/2007JD009065, 2008.

1067 Zhang, Q., Streets, D. G., Carmichael, G. R., He, K. B., Huo, H., Kannari, A.,

1068 Klimont, Z., Park, I. S., Reddy, S., Fu, J. S., Chen, D., Duan, L., Lei, Y., Wang,
1069 L. T., and Yao, Z. L.: Asian emissions in 2006 for the NASA INTEX-B mission,
1070 Atmos. Chem. Phys., 9, 5131-5153, doi:10.5194/acp-9-5131-2009, 2009.

1071 Zhang, L., Liu, L. C., Zhao, Y. H., Gong, S. L., Zhang, X. Y., Henze, D. K., Capps, S.
1072 L., Fu, T. M., Zhang, Q., and Wang, Y. X.: Source attribution of particulate
1073 matter pollution over North China with the adjoint method, Environ.Res.Lett.,
1074 10, Artn 084011 10.1088/1748-9326/10/8/084011, 2015.

1075 Zheng, B., Zhang, Q., Zhang, Y., He, K. B., Wang, K., Zheng, G.
1076 J., Duan, F. K., Ma, Y. L., and Kimoto, T.: Heterogeneous
1077 chemistry: a mechanism missing in current models to explain
1078 secondary inorganic aerosol formation during the January 2013 haze
1079 episode in North China, Atmos.Chem.Phys., 15, 2031-2049,
1080 10.5194/acp-15-2031-2015, 2015.

1081
1082

1083 **List of Figures and Table**

1084 Figure 1. Locations of 77 PM_{2.5} assimilation observation stations (black dot) and the
1085 77 independent observation stations (red triangle) in the model domain. The three
1086 colored boxes mark sub-regions with relatively dense coverage for the Beijing–
1087 Tianjin–Hebei region (JJJ, 12 assimilation stations and 12 independent stations, red
1088 box), the Yangtze River delta (YRD, 24 assimilation stations and 24 independent
1089 stations, blue box) and the Pearl River delta (PRD, 9 stations and 9 independent
1090 stations, green box).

1091
1092 Figure 2. (a) Framework of M_{SF} and (b) flow chart of the data assimilation system
1093 that simultaneously optimizes the chemical initial conditions and emissions.

1094
1095 Figure 3. Time series of prior ensemble mean RMSE and total spread for PM_{2.5}
1096 concentrations aggregated over all observations over the three sub-regions: (a)
1097 Beijing–Tianjin–Hebei region; (b) Yangtze River delta; (c) Pearl River delta; and (d)
1098 time series of the area mean ensemble spread for $\lambda_{PM2.5}$ over the three sub-regions.

1099
1100 Table 1. Comparison of the surface PM_{2.5} mass concentrations from the control and
1101 assimilation experiments to observations over all analysis times from 6 to 16 October
1102 2014.

1103
1104 Figure 4. Spatial distribution of the PM_{2.5} mass ($\mu\text{g}\cdot\text{m}^{-3}$) of the (a) observations; (b)
1105 simulation of the control run; (c) analysis of expJ; (d) analysis of expC; (e) increments
1106 of expJ; (f) increments of expC; at the lowest model level averaged over all hours
1107 from 6 to 16 October 2014.

1108
1109 Figure 5. Hourly area-averaged time series of emission scaling factors (black)
1110 extracted from the ensemble mean of the analyzed $\lambda_{PM2.5}^a$ and the corresponding
1111 analyzed unspeciated primary PM_{2.5} emissions $E_{PM2.5}^a$ (blue) over the three
1112 sub-regions: (a) Beijing–Tianjin–Hebei region; (b) Yangtze River delta; and (c) Pearl
1113 River delta.

1114
1115 Figure 6. Hourly area-averaged time series of emission scaling factors extracted from
1116 the ensemble mean of the analyzed (a) λ_{NO}^a ; (a) λ_{SO2}^a ; (a) λ_{NH3}^a over the three
1117 sub-regions: Beijing–Tianjin–Hebei region (JJJ, black), Yangtze River delta (YRD,
1118 green), and Pearl River delta (PRD, blue).

1119
1120 Figure 7. Spatial distribution of $\lambda_{PM2.5}$ at the lowest model level averaged over all
1121 hours from 6 to 16 October 2014.

1122
1123 Figure 8. Spatial distribution of (a) the prior unspeciated primary sources of PM_{2.5}
1124 ($\mu\text{g}\cdot\text{m}^{-2}\text{ s}^{-1}$) and (b) the time-averaged differences between the ensemble mean
1125 analysis and the prior values ($\mu\text{g}\cdot\text{m}^{-2}\text{ s}^{-1}$) at the lowest model level averaged over
1126 all hours from 6 to 16 October 2014.

1127

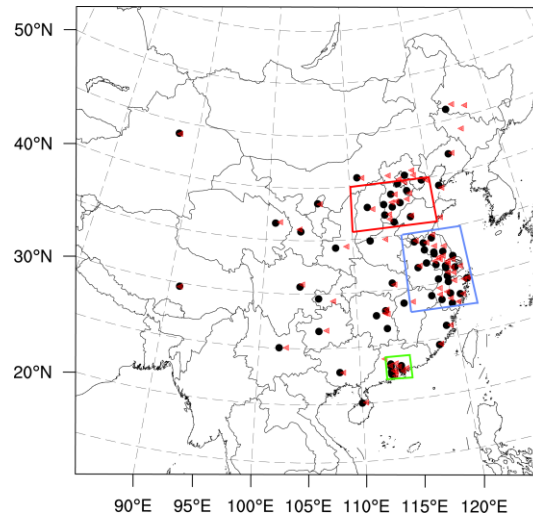
1128 Figure 9. Time series of the hourly PM_{2.5} obtained from observations (circle),
1129 analysis (blue line), control run (black line) and hourly output of 48-h forecast in three
1130 megacities: (a) Beijing; (c) Shanghai; and (e) Guangzhou in expJ and (b) Beijing; (d)
1131 Shanghai; and (f) Guangzhou in expC. See text in section 5.4.

1132

1133 Figure 10. Bias of surface PM_{2.5} as a function of forecast range calculated against
1134 independent observations over the three sub-regions: (a) Beijing–Tianjin–Hebei
1135 region; (c) Yangtze River delta; (e) Pearl River delta and RMSE over (b) Beijing–
1136 Tianjin–Hebei region; (d) Yangtze River delta; (f) Pearl River delta; (g) Normalized
1137 RMSE (assimilation divided by control) for expJ and (h) (g) Normalized RMSE for
1138 expC.

1139

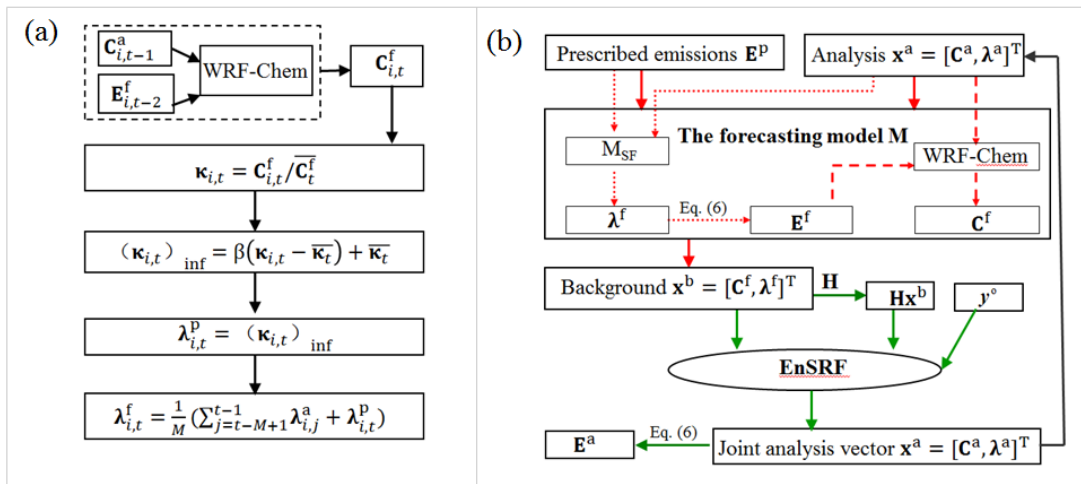
1140
1141
1142



1143
1144
1145
1146
1147
1148
1149
1150
1151

Figure 1. Locations of 77 PM_{2.5} assimilation observation stations (black dot) and the 77 independent observation stations (red triangle) in the model domain. The three colored boxes mark sub-regions with relatively dense coverage for the Beijing–Tianjin–Hebei region (JJJ, 12 assimilation stations and 12 independent stations, red box), the Yangtze River delta (YRD, 24 assimilation stations and 24 independent stations, blue box) and the Pearl River delta (PRD, 9 stations and 9 independent stations, green box).

1152



1153

1154

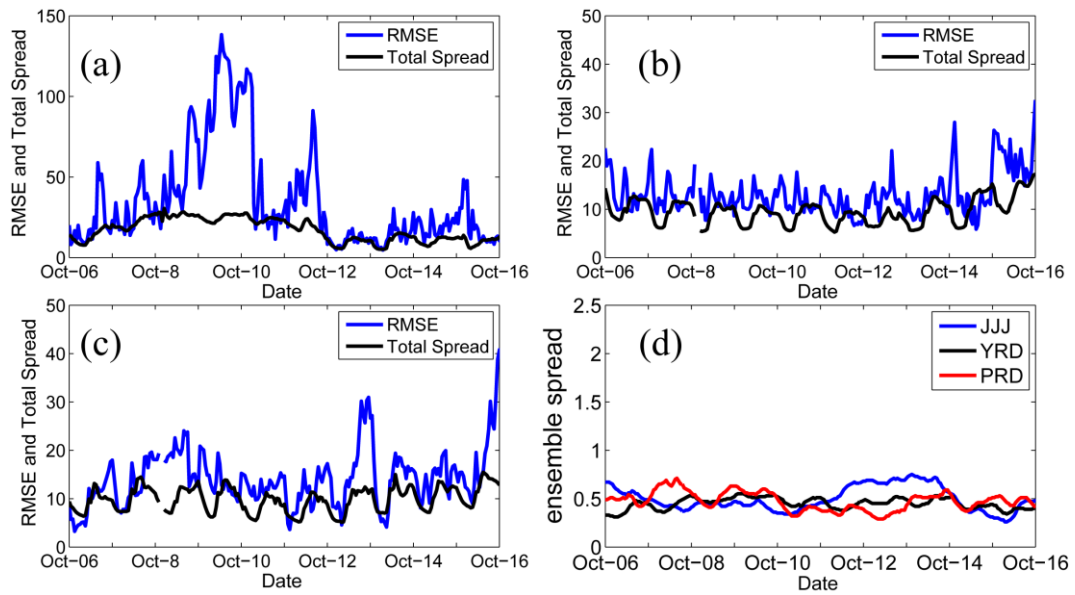
1155

1156

Figure 2. (a) Framework of M_{SF} and (b) flow chart of the data assimilation system that simultaneously optimizes the chemical initial conditions and emissions.

1157

1158



1159

1160

1161

1162

1163

1164

Figure 3. Time series of prior ensemble mean RMSE and total spread for $PM_{2.5}$ concentrations aggregated over all observations over the three sub-regions: (a) Beijing–Tianjin–Hebei region; (b) Yangtze River delta; (c) Pearl River delta; and (d) time series of the area mean ensemble spread for $\lambda_{PM_{2.5}}$ over the three sub-regions.

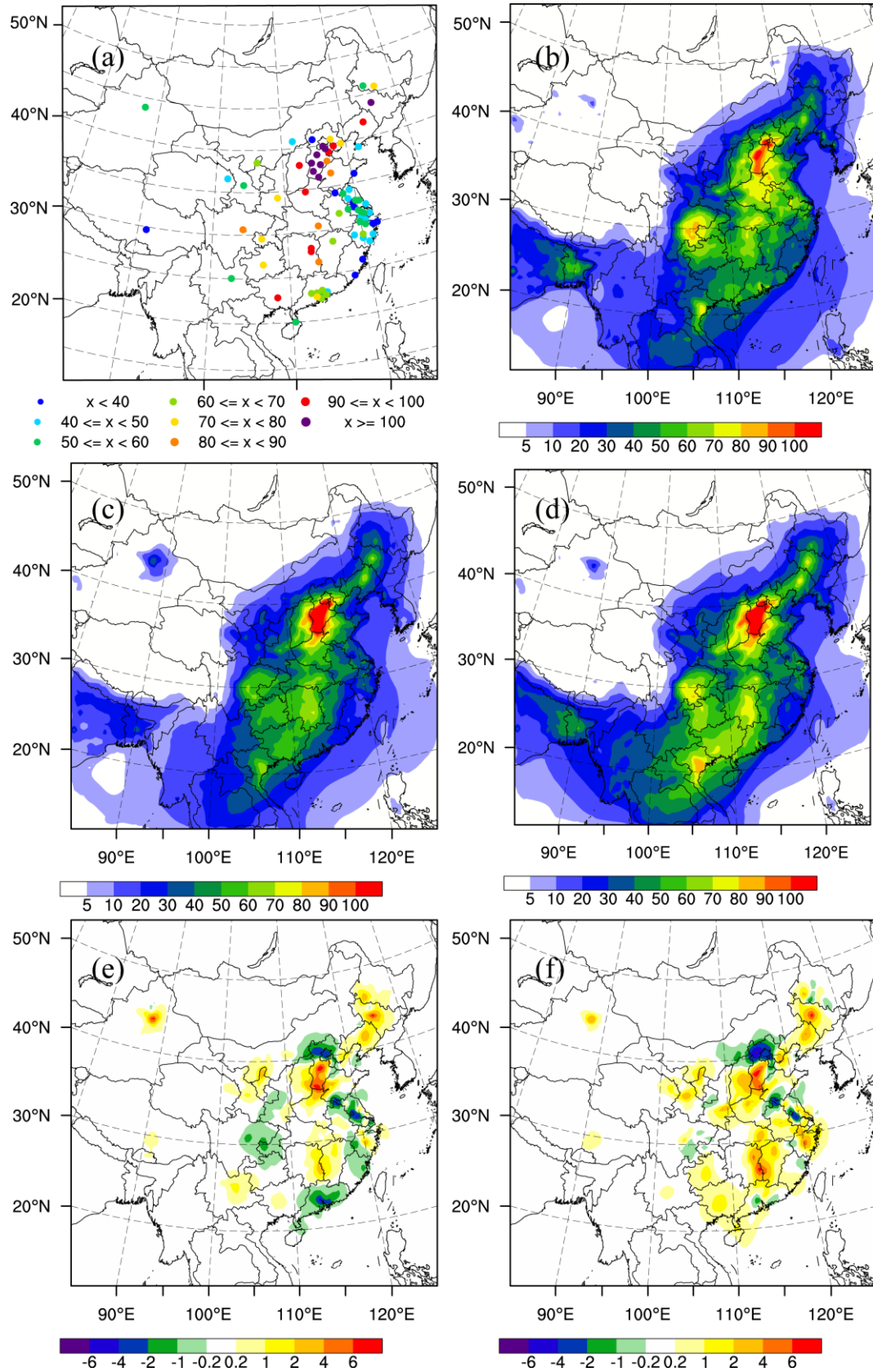
1165

1166 Table 1. Comparison of the surface PM_{2.5} mass concentrations from the control and
 1167 assimilation experiments to observations over all analysis times from 6 to 16 October
 1168 2014.

Region	Experiment	Mean	Mean	BIAS	RMSE	CORR
		observed value	simulated value			
Beijing–	Control		98.3	–18.0	81.6	0.790
Tianjin–	expJ	116.3	106.0	–10.3	66.9	0.827
Hebei	expC		104.1	–12.2	64.0	0.845
Yangtze	Control		64.4	15.9	30.6	0.593
River	expJ	48.5	46.9	–1.6	15.3	0.846
delta	expC		46.1	–2.4	17.3	0.803
Pearl	Control		82.4	20.6	31.8	0.624
River	expJ	61.8	66.5	4.7	16.1	0.800
delta	expC		64.1	–2.3	15.6	0.797

1169

1170



1171

1172

1173

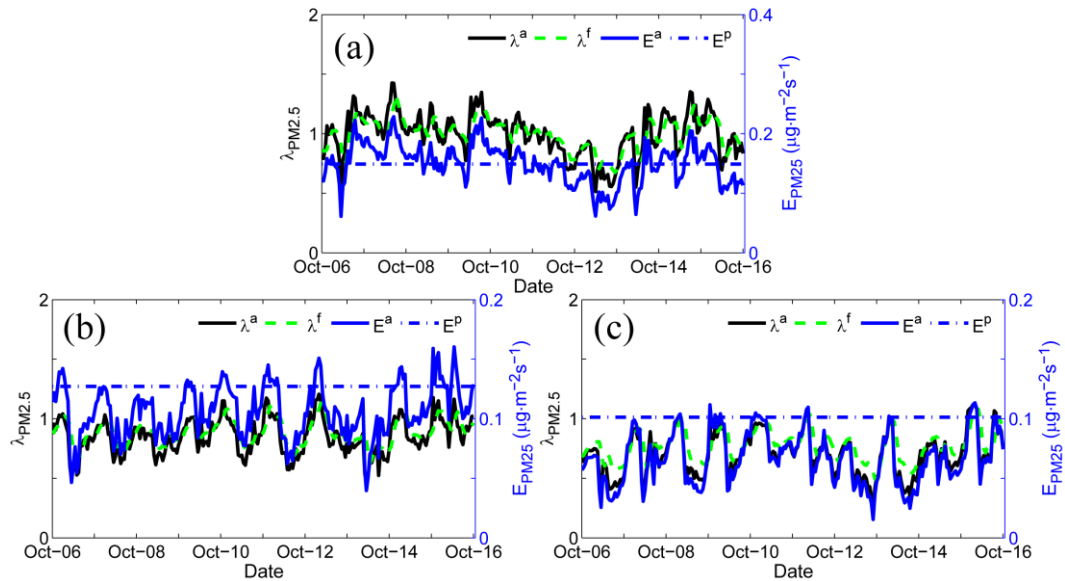
1174

Figure 4. Spatial distribution of the PM_{2.5} mass (μg m⁻³) of the (a) observations; (b) simulation of the control run; (c) analysis of expJ; (d) analysis of expC; (e) increments of expJ; (f) increments of expC; at the lowest model level averaged over all hours

1175

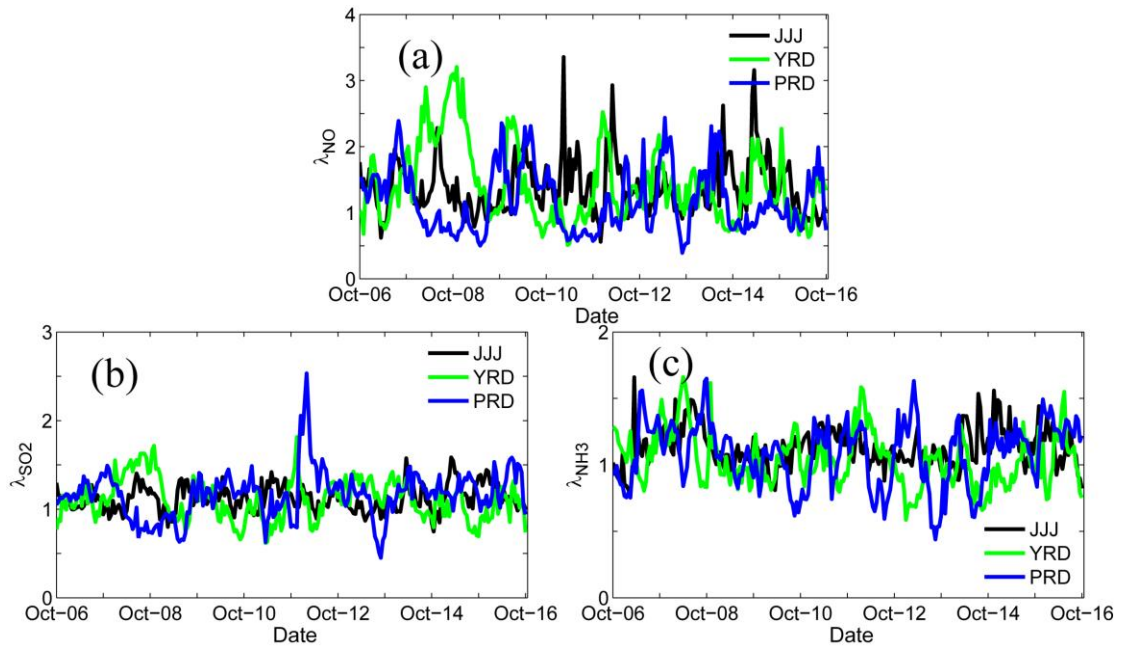
from 6 to 16 October 2014.

1176
1177
1178



1179
1180
1181
1182
1183
1184
1185

Figure 5. Hourly area-averaged time series of emission scaling factors (black) extracted from the ensemble mean of the analyzed $\lambda_{PM_{2.5}}^a$ and the corresponding analyzed unspesiated primary $PM_{2.5}$ emissions $E_{PM_{2.5}}^a$ (blue) over the three sub-regions: (a) Beijing–Tianjin–Hebei region; (b) Yangtze River delta; and (c) Pearl River delta.



1186

1187

1188

1189

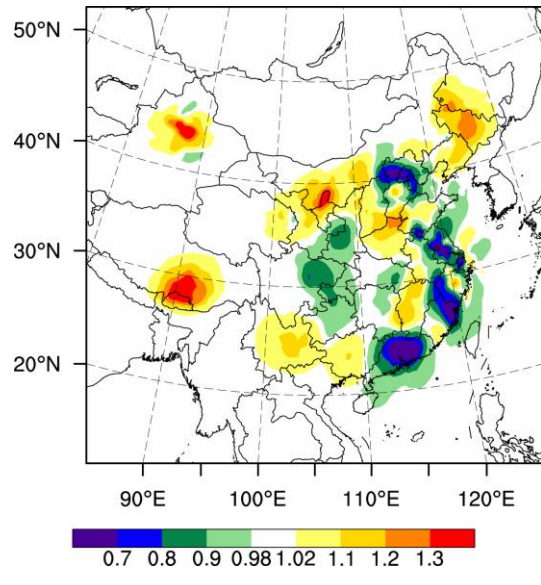
1190

1191

1192

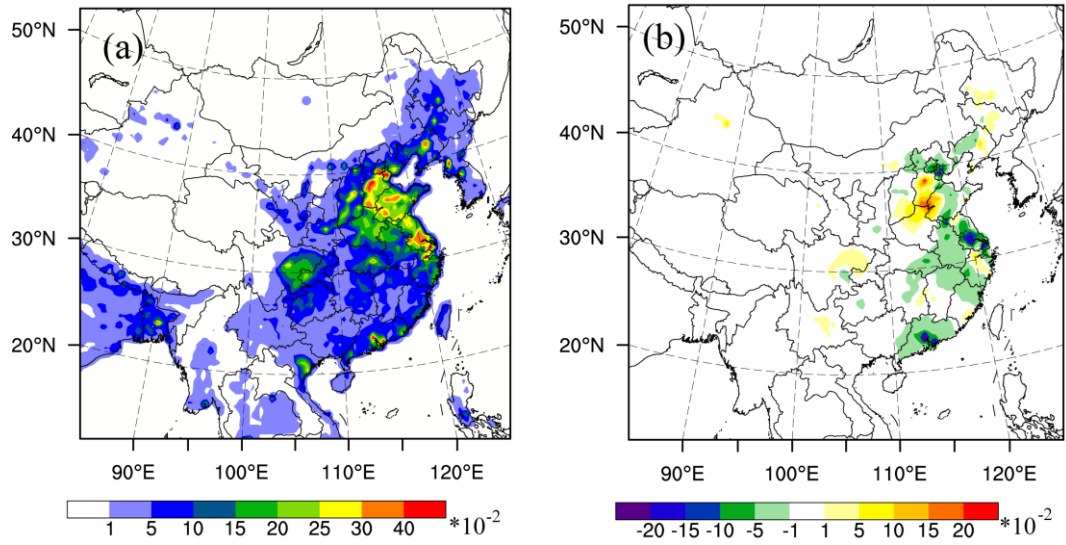
Figure 6. Hourly area-averaged time series of emission scaling factors extracted from the ensemble mean of the analyzed (a) $\lambda_{\text{NO}}^{\text{a}}$; (a) $\lambda_{\text{SO}_2}^{\text{a}}$; (a) $\lambda_{\text{NH}_3}^{\text{a}}$ over the three sub-regions: Beijing–Tianjin–Hebei region (JJJ, black), Yangtze River delta (YRD, green), and Pearl River delta (PRD, blue).

1193
1194



1195
1196
1197
1198

Figure 7. Spatial distribution of $\lambda_{PM2.5}$ at the lowest model level averaged over all hours from 6 to 16 October 2014.



1200

1201

1202

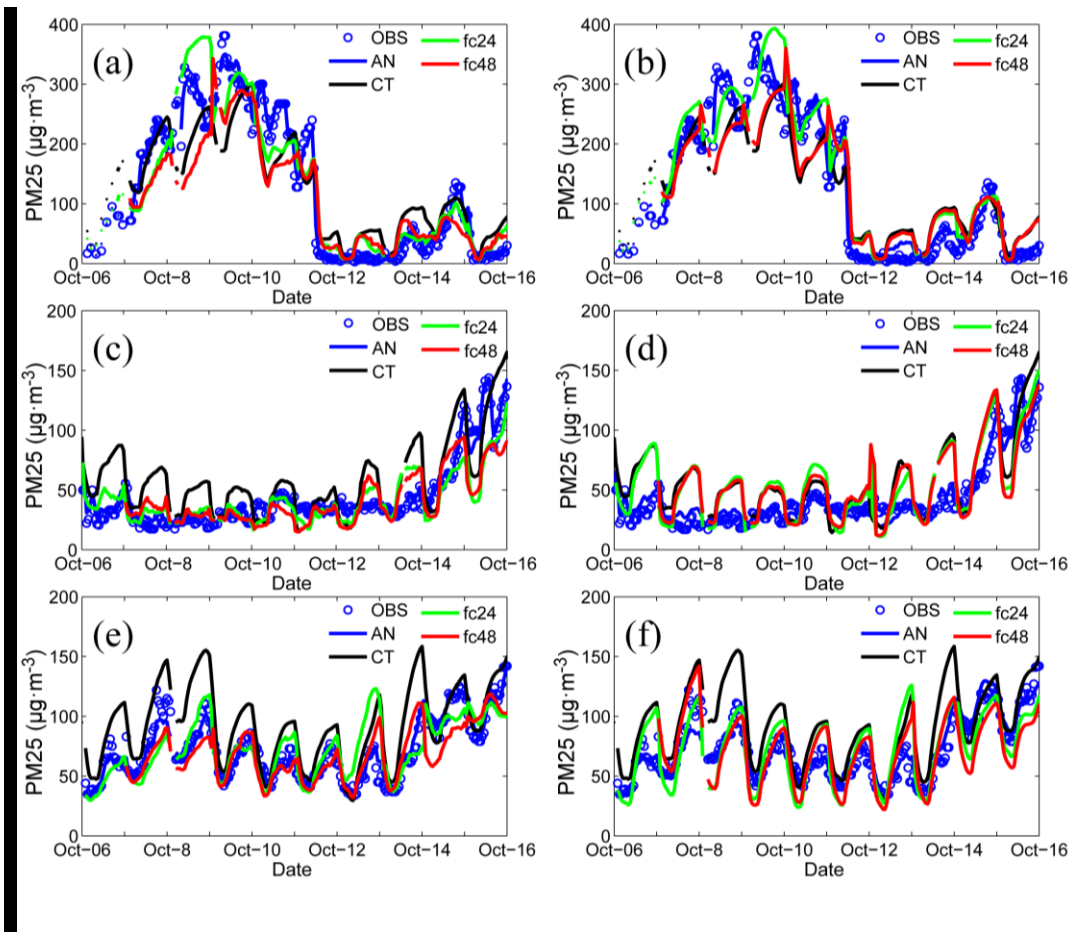
1203

1204

1205

1206

Figure 8. Spatial distribution of (a) the prior unspeciated primary sources of PM_{2.5} ($\mu\text{g m}^{-2} \text{s}^{-1}$) and (b) the time-averaged differences between the ensemble mean analysis and the prior values ($\mu\text{g} \cdot \text{m}^{-2} \text{s}^{-1}$) at the lowest model level averaged over all hours from 6 to 16 October 2014.



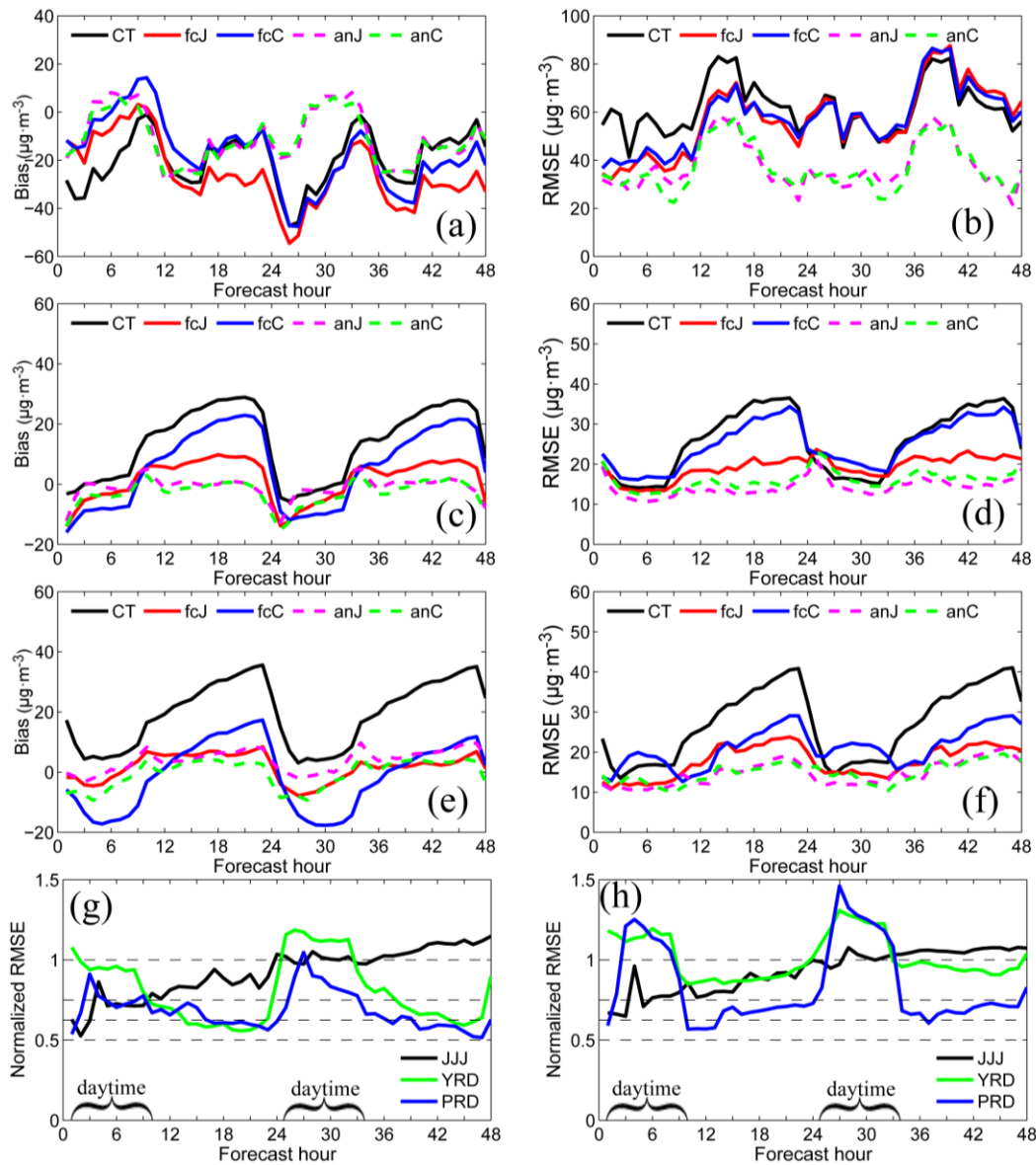
1208

1209 Figure 9. Time series of the hourly PM_{2.5} obtained from observations (circle), analysis
 1210 (blue line), control run (black line) and hourly output of 48-h forecast in three
 1211 megacities: (a) Beijing; (c) Shanghai; and (e) Guangzhou in expJ and (b) Beijing; (d)
 1212 Shanghai; and (f) Guangzhou in expC. See text in section 5.4.

1213

1214

1215



1216

1217

1218

1219

1220

1221

1222

Figure 10. Bias of surface $\text{PM}_{2.5}$ as a function of forecast range calculated against all the independent observations over the three sub-regions shown in figure 1: (a) Beijing–Tianjin–Hebei region; (c) Yangtze River delta; (e) Pearl River delta and RMSE over (b) Beijing–Tianjin–Hebei region; (d) Yangtze River delta; (f) Pearl River delta; (g) Normalized RMSE (assimilation divided by control) for expJ and (h) Normalized RMSE for expC. The statistics were computed from 6 to 16 October.